Proteostasis Landscapes of Selective versus Poorly Responsive CFTR Variants Reveals Structural Vulnerabilities to Correction

Eli Fritz McDonald[1,2], Minsoo Kim[1,3], John A Olson III[1,3], Jens Meiler[1,2,4,5,*], Lars Plate[1,6,7,*]

[1]Department of Chemistry, Vanderbilt University, Nashville, TN 37235, USA
[2]Center for Structural Biology, Vanderbilt University, Nashville, TN 37240, USA
[3]Chemical and Physical Biology Program, Vanderbilt University, Nashville, TN 37240, USA
[4]Department of Pharmacology, Vanderbilt University, Nashville, TN 37240, USA
[5]Institute for Drug Discovery, Leipzig University, Leipzig, SAC 04103, Germany
[6]Department of Biological Sciences, Vanderbilt University, Nashville, TN 37240, USA
[7]Department of Pathology, Microbiology and Immunology, Vanderbilt University Medical Center, Nashville, TN 37232, USA

* Corresponding authors: JM (jens@meilerlab.org), LP (lars.plate@vanderbilt.edu)

ABSTRACT

Cystic Fibrosis (CF) is a lethal genetic disorder caused by variants in CF transmembrane conductance regulator (CFTR). Many disease variants are treatable with corrector compounds, which enhance the folding and trafficking of CFTR. However, correctors fail to elicit a response for every CFTR variant. Approximately 3% of persons with CF harbor poorly responsive CFTR variants. Here, we reveal that a group of poorly responsive variants overlap with selectively responsive variants in a critical domain interface (nucleotide-binding domain 1/intracellular loop 4 – NBD1/ICL4). Affinity purification mass spectrometry proteomics was used to profile the protein homeostasis (proteostasis) changes of CFTR variants during corrector treatment to assess modulated interactions with protein folding and maturation pathways. Responsive variant interactions converged on similar proteostasis pathways during correction. In contrast, poorly responsive variants subtly diverged, revealing a partial restoration of protein quality control surveillance and a capacity to correct some mutations. Computational structural modeling showed that corrector VX-445 failed to confer enough NBD1 stability to poorly responsive variants. NBD1 secondary stabilizing mutations rescued poorly responsive variants, revealing structural vulnerabilities in NBD1 required for treating poor responders. Our study provides a framework for discerning the underlying protein quality control and structural defects of CFTR variants not reached with existing drugs. These insights can help expand therapeutics to all susceptible CFTR variants to enhance personalized medicine efforts.

INTRODUCTION

Cystic Fibrosis is a lethal genetic disease caused by mutations in Cystic Fibrosis Transmembrane Conductance Regulator (CFTR), an epithelial anion channel. Mutant CFTR leads to a lack of anion transport in the lung epithelia, dysfunctional cilia transport of mucus, mucus build-up, infection, and eventually death. The current treatment strategy for CF involves small molecule therapeutics that either elevate CFTR channel activity (potentiators) or bolster CFTR folding stability (correctors)[1]. Correctors were originally developed to treat the most common CFTR variant, the deletion of phenylalanine at position 508 (F508del), which misfolds. Beyond F508del, the FDA has expanded and approved the combination therapy of two correctors (VX-661 & VX-445) and one potentiator (VX-770) for 183 other CF-causing variants[2,3]. CFTR variant response is defined by surface trafficking, plasma membrane (PM) expression, and functional rescue of anion conductance. Treatable variants respond differently to mechanistically distinct correctors, demonstrating *selective response* and creating a need for rational combinatorial therapies guided by variant-specific drug response profiles[2]. Despite the revolution in CF treatments, ~10% of persons with CF remain untreated[4]. Among the untreatable population, ~3% harbor Class-II, misfolding-prone variants potentially targetable with correctors. However, sparse biochemical research on the mechanisms of action underlying variant response and non-response has hindered progress toward therapeutic expansion to reach poorly responsive variants.

CFTR is an ABC transporter-type protein comprised of two nucleotide-binding domains (NBDs), two transmembrane domains (TMDs), and an unstructured R domain (RD)[5]. Correctors are classified by their capacity to stabilize a domain or a domain interface. For example, VX-661 binds TMD1[6] and stabilizes the TMD/NBD1 interface (Type-I corrector)[7]. By contrast, VX-445 binds to the interface of TMD2 and the N-terminal lasso motif[8] to allosterically stabilize NBD1 (Type-III corrector)[7,9]. Type-II correctors stabilize NBD2, although none are FDA-approved to date[7]. A deep mutational scan (DMS) of 129 CFTR variants recently revealed VX-445 selective variants L165S, Y1032C, T1036N, H1054D, and R1066H[10]. The latter four variants localized proximate to the VX-445 binding site[8] in transmembrane helix 10 (TH10) of TMD2. Likewise, VX-661 selective variants such as P67L and Q98R reside in TMD1 near the VX-661 binding site[10]. These results suggested that correctors stabilize structural defects proximate to their binding pocket and imply proximity drives selective response.

Additionally, protein homeostasis (proteostasis) is important for the selective response. Misfolding variants such as F508del continually cycle through molecular chaperones and proteostasis factors, which direct CFTR to degradation machinery, leading to low CFTR accumulation at steady state[2,11,12]. We developed a multiplexed quantitative interactomics platform for measuring changing CFTR interactions with protein homeostasis machinery or *proteostasis landscapes*[13,14]. Our platform demonstrated that VX-809 (a VX-661 analog) altered P67L proteostasis between folding and proteasomal degradation compared to F508del, allowing P67L to escape degradation and selectively respond to VX-809[13]. Additionally, proteostasis changes can turn a poor-responder into a responder: we found modulation of translational dynamics by knockdown of specific ribosomal subunit proteins can sensitize P67L to respond to VX-445[14]. Thus, correctors modulate CFTR proteostasis along specific pathways in addition to stabilizing proximate structural defects.

Besides demarcating selectively responsive variants, the DMS study revealed several poorly responsive variants, such as V520F, L558S, A559T, R560T, A561E, Y569D, and R1066C[15]. Previously, research has focused little on these variants because of their low allele frequency (**Supplemental Table S1**). However, a few previous *in vitro* studies have also demonstrated no or mild response among these variants[9,16–19]. Importantly, small molecules and stabilizing mutations had varying effects on different poor responders, indicating different capacities for correction. Thus, we sought to understand the proteostatic and structural deficiencies of poorly responsive variants to reveal commonalities, disparities, and potential vulnerabilities to correction.

Here, we used quantitative multiplexed interactomics to measure and define the proteostasis landscapes of five VX-445 selectively responsive variants – L165S, Y1032C, T1036N, H1054D, and R1066H - and seven poorly responsive variants – V520F, L558S, A559T, R560T, A561E, Y569D, and R1066C. We found responsive variants experience divergent basal interactions with proteostasis pathways, but these proteostasis landscapes convergent under VX-445 treatment. By contrast, poorly responsive variants showed subtly different proteostasis

changes during dual VX-661 and VX-445 drug treatment. Poor responders R560T and Y569D were corrected towards productive proteostasis interactions in early biogenesis pathways. Meanwhile, regardless of correction, poor responders L558S, A559T, and A561E remained trapped in the same proteostasis interactions. These discoveries point to a partial restoration of protein quality surveillance for some variants, yet these alterations remain insufficient to enhance CFTR surface trafficking. Computational structural simulations in Rosetta showed that VX-445 primarily stabilizes CFTR by correcting defects in ICL4 over NBD1 in responders and poor responders. This led us to hypothesize that increased NBD1 stabilization with secondary mutation might rescue poorly responsive variants. Indeed, the I539T substitution successfully rescued A559T, R560T, and Y569D in combination with correctors. This suggests NBD1 targeting correctors may be required to treat poorly responsive variants, paving a clear path forward for persons with CF without therapeutic options. Thus, our proteostasis landscape profiling and structural modeling revealed subtle variations in the drug response mechanism of poorly responsive CFTR variants, which may guide future studies to characterize drug susceptible variants for genetic diseases.

RESULTS

I. Selectively responsive and poorly responsive CFTR variants contact at the NBD1/ICL4 ATPase core interface

While some CFTR variants respond promiscuously to intermolecular interactions bestowed by corrector binding, others demonstrate a selective response to one corrector over the other. A deep mutational scan (DMS) study of CFTR compared VX-661 and VX-445 treatments and revealed selectively responsive variants with increased surface CFTR trafficking[10]. This dataset revealed P5L, L165S, Y1032C, T1036N, H1054D, R1066H, and L1077P selectively respond to VX-445 and P67L, R75Q, Q98R, and V201M selectively respond to VX-661 (**Supplemental Figure S1A**). The proximity of the mutations in the selectively responsive variants to the VX-445 and VX-661 respective binding sites[6,8] (**Supplemental Figure S1B**) led to the paradigm that local intermolecular interactions may drive the selective response.

The DMS study also revealed a suite of poorly responsive variants (<30 %WT, **see Methods**) that failed to increase cell surface trafficking in response to dual corrector treatment (**Figure 1A**). We filtered the DMS data against the variants FDA-approved for VX-445 and VX-661 to reveal two hotspots where unapproved, poorly responsive variants have amino acid changes in the structure[3] (**Figure 1B**). A collection of such sites in poor responders is found at the transition from the alpha-helical subdomain to the ATPase subdomain of NBD1 (**Figure 1C**) (L558S, A559T, R560T/K, A561E, and Y569D). The other collection of sites is found in the intercellular loop 4 (ICL4) region of TMD2 (L1065P and R1066C). Although far in sequence, these variants contact each other in the three-dimensional folded CFTR structure at the NBD1/ICL4 interface (**Figure 1D**).

To corroborate these findings, we filtered a larger CFTR variant drug screening study[20] from Bihler et al. against the FDA-approved list[3]. Although this study included channel activity, we considered trafficking efficiencies to focus on misfolding/mis-trafficking variants. This revealed an expanded collection of unapproved and poorly responsive variants also localized in NBD1 and ICL4 (**Figure 1E**). Additional poorly responsive variants occur in the lasso motif, the N-terminus of TMD1, the middle of TMD2, and NBD2. Finally, since F508del folds at lowered temperature[21], we filtered a temperature sensitivity screen from Anglés et al. against the FDA-approved list[16] (**Figure 1F**). Poor responders V520F, R560T, R560K, and L1065P were rescued by temperature correction. Other variants, such as L558S, A559T, Y569D, and R1066C, responded poorly to temperature correction. Differential temperature correction profiles indicated that poorly responsive variants diverge in their rescue susceptibility. Divergent rescue susceptibility may stem from subtly divergent proteostasis and structural defects. These analyses unveiled collections of poorly responsive variants, particularly in NBD1 and ICL4.

To confirm the selectively responsive and poorly responsive nature of CFTR variants of interest, we tested these variants in a HEK293T transient expression system. Briefly, we generated CFTR expression plasmids encoding WT and variants to transiently transfect into HEK293T cells and treat for 24 h with 3 μM VX-661, 3 μM VX-445, 3 μM VX-445 + 3 μM VX-661 combination, or DMSO vehicle. Lysates were resolved via SDS-PAGE and immunoblotted for CFTR. All VX-445 selective variants (L165S, Y1032C, T1036N, H1054D, and R1066H) demonstrated robust rescue of mature CFTR by VX-445 and a moderate response to VX-661 as indicated by the higher molecular weight C-band (**Figure 1G**). Quantification and statistical comparison of VX-445 versus VX-661 trafficking efficiency confirmed VX-445 selective response for all variants but Y1032C, which was promiscuously responsive (**Figure 1G**). Thus, we conclude these variants are robustly responsive in our transient expression system.

Comparing dual drug treatment to DMSO, poorly responsive variants L558S, A559T, R560T, A561E, and Y569D showed no trafficking efficiency increase (**Figure 1H**). V520F and R1066C, by contrast, demonstrated statistically significant trafficking efficiency increase with dual drug treatment albeit with <50% WT expression and less than F508del (**Figure 1H**). These data suggest the effective responsiveness and poor responsiveness of our variants of interest are robust and reproducible in our transient expression systems, amenable to multiplexed quantitative interactomics to characterize the proteostasis interactions.

II. Interactome remodeling of responsive and poorly responsive CFTR variants diverge

We integrated our previously established affinity purification mass spectrometry (AP-MS) approach with 18-plex tandem mass tags (TMT) for increased multiplexing to quantify relative interactor levels across CFTR variants and drug conditions[13] (**Figure 2A**). We collected and compared two interactomics datasets – selectively responsive variants with VX-445 correction and poorly responsive variants with VX-661 and VX-445 dual drug correction.

Briefly, HEK293T cells were transiently transfected with CFTR expression plasmids and treated with correctors or vehicle. Lysates were immunoprecipitated for CFTR and interactors with anti-CFTR monoclonal antibody-conjugated Sepharose beads. Proteins were eluted, digested, TMT labeled, and samples pooled for LC-MS/MS analysis (**Figure 2A**). Quantitative comparisons were performed after the median normalization of TMT intensity to remove non-specific interactors (**Supplemental Figure S2A-B, see Methods**). Interactors were identified by statistically comparing CFTR affinity purification protein levels to mock transfection control protein levels to remove non-specific proteins bound to the beads.

First, we determined the interactomes of five VX-445 selectively responsive variants (**Figure 2B**). We included L165S (n=5), Y1032C (n=6), T1036N (n=6), H1054D (n=6), R1066H (n=5) in our AP-MS analysis all with ± VX-445 conditions (**Supplemental Dataset S1**). A mock transfection (n=7), WT CFTR (n=7), and F508del ± VX-445 (n=5) were included as controls. WT and F508del CFTR demonstrated enrichment of bait protein and previously well-characterized interactors such as calnexin (CANX)[22,23] (**Supplemental Figure S2C-D**). By contrast, L165S showed little interactor enrichment (**Supplemental Figure S2E**). The TH10 variants Y1032C, T1036N, H1054D, and R1066H showed enrichment of CFTR and previously identified interactors such as CANX[22,23] and NHERF1[24] (**Supplemental Figure S2F-I**). VX-445 elevated CFTR levels for each variant with a similar number of interactors identified (**Supplemental Figure S3A-F**). We compiled all identified interactors of statistical significance for each selectively responsive variant into a master list comprising 655 interactors.

Next, an identical procedure was performed for seven poorly responsive variants to define their proteostasis landscapes using our multiplexed quantitative proteomics (**Figure 2C**). We opted to treat poorly responsive variants with the combination of VX-661 and VX-445 (3μM each) to investigate whether poorly responsive variants exhibit any degree of proteostasis remodeling. We included V520F (n=5), L558S (n=6), A559T (n=5), R560T (n=6), A561E (n=6), Y569D (n=5), and R1066C (n=6), and ± VX-445/VX-661 conditions for all variants in our multiplexed AP-MS analysis (**Supplemental Dataset S1**). A mock transfection (n=6), WT CFTR (n=6), and F508del ± VX-44/661 (n=6) were included as controls.

Again, we median-normalized TMT intensities before quantitative comparison to remove non-specific interactors (**Supplemental Figure S4A-B, see Methods**). WT and F508del CFTR samples showed enriched bait protein and previously identified interactors CANX[22,23], BAG2[25,26], and RNF5[27], as well as new interactor RPS27A, a small ribosomal subunit protein involved in ribosomal quality control[28,29], and LIMK2, and serine kinase implicated in actin filament assembly and Rho GTPase signaling[30,31] (**Supplemental Figure S4C-D**). Interestingly, interaction with CANX[3], BAG2, RNF5, and LIMK2 were remarkably consistent for poorly responsive variants (**Supplemental Figure S4E-K**). Treatment with VX-445/VX-661 failed to change interaction intensities compared to the vehicle (**Supplemental Figure S5A-H**). Again, we compiled identified interactors of statistical significance for each poorly responsive variant into a master list comprising 284 interactors.

Overall, the poorly responsive variants revealed a relatively small number of interactors compared to the VX-445 selectively responsive variants, although we observed an overlap of 105 shared core interactors between both datasets (**Figure 2D**). These data suggest selectively responsive and poorly responsive variants share core interactions but experience unique perturbations resulting from differential responses to the correctors. Thus, our quantitative interactomics profiling platform robustly identified CFTR interactors with and without correction across two experimental conditions, including selectively responsive and poorly responsive CFTR variants. We leveraged these interactomics datasets to understand the proteostasis landscapes of CFTR variants during correction.

III. VX-445 attenuates aberrant interactions across proteostasis pathways for selectively responsive variants

Mutation sites in the VX-445-selective CFTR variants clustered near the VX-445 binding pocket, yet how VX-445 alters the proteostasis landscapes of these variants or even F508del remains unexplored[32]. Previously, we showed that a different corrector (VX-809) altered P67L proteostasis between protein folding and proteasomal degradation, and proteostasis modulation can sensitize a poorly responsive variant to VX-445 correction[13,14]. These studies suggest a reciprocal relationship where proteostasis states drive correction susceptibility, and correction modulates proteostasis. Although VX-445 binds distinctly from VX-809 and VX-661, both corrector types likely stabilize structural defects proximate to their binding pocket[6,8,10]. Hence, we determined the interactomes of VX-445 selectively responsive variants to map the proteostasis landscapes responsible for VX-445 selectivity.

First, we sought to understand the proteostasis interactome commonalities and differences amongst the VX-445 selectively responsive variants. Interactors were organized into biological pathways annotated based on Gene Ontology (GO) terms (**Supplemental Dataset S3**) and filtered down to 170 interactors involved in protein homeostasis pathways such as translation, protein folding, proteasomal and autophagy degradation, trafficking, and endocytosis. We plotted a cluster-map of the pairwise Spearman-ranked ordered correlation coefficients between all pairs of variants and conditions (**Figure 3A, Supplemental Dataset S2**). K-means clustering split variants and conditions into four clusters (elbow method) (**Supplemental Figure S6A**). These four clusters grouped 1) WT with T1036N 2) L165S, 3) F508del with R0166H, and 4) Y1032C with H1054D (**Figure 3A**). Clustering suggests VX-445 restores T1036N interactome the most towards WT, whereas R1066H likely experiences similar interactions to F508del. To gain further insights into interactome remodeling with correctors, we investigated the individual protein level changes to determine the pathways involved in the rescue.

We compared the log2 fold change of individual protein interactors across the conditioned using the WT condition as a reference point. The resulting heatmap revealed that VX-445 decreased interactions across all variants, with Y1032C and T1036N displaying the largest changes (**Figure 3B, Supplemental Dataset S4**). Additionally, selectively responsive variants interact with a diverse suite of ribosomal subunits, proteasomal subunits, co-chaperones such as DNAJB4/6, trafficking factors such as COG2/6 and EXOX2/3/4/6/8, and endocytosis machinery such as HAX1. VX-445 decreased interactions with previously characterized CFTR folding and degradation factors (**Figure 3B**) such as CANX[22,23,33], BAG2[25,26], DNAJB2[34], FKBP4/8[35], PSMC3[13], Hsp70[36,37], Hsp90[12,38,39] isoforms, and NHERF1 - a plasma membrane (PM) scaffolding protein important for CFTR peripheral stability and quality control[24]. R1066H portrayed a unique basal state proteostasis landscape with a marked increase in interactions with translation machinery, suggesting co-translational evaluation is important for R1066H (**Figure 3B**).

We plotted the distribution of interaction changes for individual pathways to gain insights into how VX-445 modulates proteostasis pathways in aggregate. For clarity, we show two violin plots, one of F508del, T1036N, and R1066H interaction changes and one of L165S, Y1032C, and H1054D interaction changes (**Figure 3C, Supplemental Dataset S5**) in both the basal and VX-445 treated conditions. The CFTR-relevant proteostasis pathways were arranged in approximate order of biogenesis: translation, folding, proteasomal degradation, lysosomal degradation/autophagy, trafficking, and endocytosis - although we note that these processes occur simultaneously in cells. VX-445 significantly decreased interactions across all proteostasis pathways for selectively responsive variants L165S, Y1032C, T1036N, H1054D, and R1066H (**Figure 3C**).

Surprisingly, VX-445 failed to alter F508del interactions with any proteostasis pathways (**Figure 3C**). A waterfall plot of individual log2 fold changes between treated and basal conditions revealed the upregulation of late biogenesis pathway proteins such as endocytosis proteins SPART, CHMP5, and HAX1 and trafficking proteins VAMP7, COG6, and RTN3 (**Figure 3D**). Conversely, VX-445 downregulated endocytosis factors GGA1 and CORO1A (**Figure 3D**). This suggests VX-445 may modulate F508del interactions with endocytosis factors in later-stage biogenesis.

To distinguish a possible role for later-stage biogenesis in F508del specifically, we plotted individual endocytosis pathway correlation between DMSO and VX-445 for F508del, R1066H, and T1036N (**Figure 3E**).

The best-fit lines (colored dotted) showed distinct off-axis divergence. VX-445 diverted F508del and T1036N endocytosis factors more than R1066H, suggesting endocytosis may play a role for these variants. Indeed, endocytosis represents the most diverted F508del pathway among proteostasis pathways (**Supplemental Figure S6B-F**).

The comparative interactomic profiling of VX-445 selective variants provided several key insights into the proteostasis landscape governing VX-445 response. First, basal state proteostasis landscapes are distinct among VX-445 selective responders. Second, despite the difference in basal proteostasis states, pathway-level interaction changes appear similar across variants. All interactions within relevant pathways decreased, suggesting structural stabilization may drive selective response instead of specific altered proteostasis pathways. Last, F508del proteostasis is differently modulated by VX-445 compared to VX-809[13] in a manner consistent with VX-445 acting later and VX-809 acting early in F508del biogenesis[6]. Thus, VX-445 can rescue at multiple points in the pathway in a mutation-dependent manner.

IV. Correctors guide poorly responsive CFTR variants toward productive proteostasis landscapes

Because of poor genetic sampling amongst underrepresented and/or low-income populations and subsequent low-measured allele frequency, poorly responsive CFTR variants remain historically understudied, and their biogenesis defects remain unclear. Thus, we used our quantitative multiplexed interactomics platform to study seven poorly responsive CFTR variants.

To understand the proteostasis interactome commonalities and disparities amongst the poorly responsive variants, we again filtered the interactors for 65 proteins involved in protein homeostasis (**Supplemental Dataset S3**). Then, we plotted a cluster-map of pairwise Spearman rank-ordered correlation coefficient between all variants and conditions for 65 proteostasis interactors (**Figure 4A, Supplemental Dataset S2**). K-means clustering splits variants and conditions into 5 clusters (elbow method) (**Supplemental Figure S7A**). These clusters grouped F508del + VX-445/661 with WT as well as Y569D, R1066C, and A561E together regardless of treatment. R560T in the basal condition clustered with L558S and A559T + VX-445/661. Conversely, L558S in the basal condition clustered with R560T + VX-445/661. The largest cluster was formed from basal state F508del, V520F, and A559T along with V520F + VX-445/661. These results suggest poorly responsive variants exhibit diverse proteostasis landscapes distinct from WT and each other.

Next, we compared the log2 fold change of individual interactor levels across each variant using WT CFTR as the reference points and organizing relevant proteostasis pathways proteins by GO terms (**Supplemental Dataset S3, Figure 4B, Supplemental Figure S4**). Consistent with the poorly responsive nature of these variants, we observed minimal change across most of the proteostasis interactomes when treated with VX-661 and VX-445 compared to the vehicle. Several previously known interactors were identified, such as CANX[22,23,33], BAG2[25,26], BAG5[40], Hsp90AB1[38], RNF5[27], and RNF185[41]. Additionally, proteostasis interactors involved with translation, protein folding, proteasomal degradation, autophagy, lysosomal pathway, trafficking, and endocytosis were also identified. Thus, important CFTR proteostasis interactors were identified in our poorly responsive dataset.

To determine if combination drug treatment modulated specific proteostasis pathways for the distinct CFTR variants, we again plotted the aggregate distribution changes as violin plots (**Figure 4C Supplemental Dataset S6**), arranging CFTR-relevant pathways by approximate order of biogenesis: translation, folding, proteasomal degradation, lysosomal degradation/autophagy, trafficking, and endocytosis. Consistent with our prior studies with VX-809 treatment[13], VX-661 and VX-445 decreased F508del interactions with translation, protein folding, and proteasomal degradation factors (**Figure 4C**). In contrast to VX-809 treatment alone, dual treatment with VX-661 and VX-445 attenuated F508del interactions with lysosomal degradation and autophagy machinery.

We were surprised to reveal some subtle yet significant remodeling of proteostasis interactions for the poorly responsive variants. Like our observations in F508del, dual treatment attenuated V520F interactions with translation, protein folding, and lysosome/autophagy machinery. On the other hand, R560T displayed decreases in interactions with protein folding and proteasomal degradation factors (**Figure 4C**), suggesting R560T may get

caught in a degradation bottleneck rather than during co-translational folding. Dual corrector treatment decreased Y569D interactions with translation and protein folding proteins while decreasing Y569D and R1066C interactions with proteasomal degradation machinery (**Figure 4C**). By contrast, the dual correctors failed to alter L558S, A559T, and A561E proteostasis pathway interactions, indicating these variants remain in a *trapped* proteostasis state even with correctors.

To determine any interaction changes among variants in trapped proteostasis states, we plotted a waterfall plot of log2 fold changes between treated and basal conditions for L558S, A559T, and A561E, with F508del as a control for reference (**Supplemental Figure S7B-E**). Interestingly, drug treatment decreases L558S and A561E interactions with autophagy protein SH3GLB1 (**Supplemental Figure S7C, S7E**), but increases A559T interactions with SH3GLB1 (**Supplemental Figure S7D**) – which may recruit proteins to membranes with high curvature and promote membrane fusion[42]. This suggests dual correction pushes L558S and A561E to a proteostasis checkpoint that A559T reaches without correction.

To further illustrate the stratification of proteostasis states, we generated a spider plot highlighting the significance of the change in proteostasis pathway interactions, as -log10 p-values, for each poorly responsive variant (**Figure 4D**). R560T and Y569D demonstrate a distinct pattern of altered interactions with proteasomal degradation and folding machinery, whereas V520F shows altered interactions with autophagy/lysosomal and translation proteins (**Figure 4D**). This further demonstrates that several poorly responsive variants escape different proteostasis interactions during correction and are being guided toward *productive*, pro-folding, and trafficking proteostasis states.

Interactomics profiling of poor responders revealed previously hidden insight into the proteostasis landscapes that may prevent corrector rescue. Poorly responsive variants are refractory to combination treatment-induced remodeling of the interactome towards that of WT. F508del early biogenesis pathway interactions are uniquely restored in the presence of both VX-661 and VX-445 compared to the changes caused by VX-809[13] or VX-445 alone. The dual corrector treatment attenuated poorly responsive variant interactions distinctly for each variant and only early in biogenesis. Despite lacking mature CFTR rescue, correctors guided R560T and Y569D towards productive proteostasis states with overlapping pathways remodeled, suggesting these variants may share commonalities in correctability.

V. VX-445 fails to correct NBD1 structural defects in trapped proteostasis poor responders

The distinct proteostasis landscapes of the nonresponsive variants prompted us to interrogate their structural defects to assess how destabilizing regions of CFTR contribute to differential proteostasis recognition. Prior focus on Type-I corrector simulations[15,43] inspired us to pursue variants bound with VX-445. Experimentally determined CFTR structures are only available for one variant – F508del. Hence, understanding the structural defects of variants is only tractable with computational modeling approaches. Using our previously established[43] and applied[10] Rosetta Comparative Modeling (RosettaCM) method, developed specifically for CFTR modeling and benchmarked against experimental CFTR thermodynamic data[44–47], we simulated poorly responsive variants in two conformations in the apo and VX-445 bound state.

Briefly, we refined an ensemble of CFTR models into active (PDB 6MSM)[48] and inactive (PDB 5UAK)[49] CFTR cryo-EM density maps using automated refinement in Rosetta[50]. We then selected the lowest scoring models in terms of Rosetta score and docked VX-445 to a binding pocket determined by Cryo-EM[8]. We used the same coordinates as the docked models for the apo models but removed the VX-445 atoms so that energetic calculations would be directly comparable. Then, we mutated the respective residues (V520F, L558S, A559T, R560T, A561E, Y569D, and R1066C) in the apo and VX-445 docked models. In silico mutagenesis was performed for both the active and inactive state and followed by RosettaCM to generate 1000 structural models of each mutation in the active and inactive conformations.

To determine which variants were stabilized by VX-445, we plotted the Rosetta score of the 100 lowest-scoring apo models (10% of the total generated models) against the lowest-scoring 100 VX-445 models (**Figure 5A-B, Supplemental Dataset S7**). Variants falling below the normal dotted line representing x=y indicate thermodynamic stabilization by VX-445, whereas variants above the line are destabilized, and variants on the line

remain unchanged. VX-445 globally stabilized poorly responsive variants in the active conformation (**Figure 5A**). By contrast, in the inactive conformation, VX-445 only stabilized V520F, Y569D, and R1066C (**Figure 5B**). Variants L558S, A559T, R560T, and A561E showed no significant change in Rosetta score when bound to VX-445 in the inactive state (**Figure 5B**).

We next sought to understand what structural defects contributed to variant instability and if VX-445 corrected defects. First, we mapped onto the inactive structure (5UAK) the ensemble change in root-mean-square deviation (ΔRMSD) between WT and Y569D apo state, which represents the instability caused by the variant (**Figure 5C**). We compared it to the ΔRMSD between the apo and VX-445 bound state, representing the stability conferred by VX-445 to the variant (**Figure 5C**). Here, a large positive ΔRMSD (red) suggests destabilizing effects of mutation, whereas a large negative ΔRMSD (blue) suggests stabilizing effects of VX-445. NBD1 residues 485-572 were quantified because these residues contact TMD2 via ICL4. The ΔRMSD values were summed across the region and rolled in a bar plot to easily compare the variant instability versus VX-445 conferred stability (**Figure 5D**).

To understand whether structural defects differed between the poor responders in productive vs. trapped proteostasis states, we plotted ΔRMSD for each group of variants (**Figure 5E-F, Supplemental Figure S8**). VX-445 reduced the NBD1 ΔRMSD for productive proteostasis variants V520F, R560T, and Y569D (**Figure 5E**), while either failing to reduce or increasing NBD1 ΔRMSD for the trapped proteostasis variants (**Figure 5F**). This suggests NBD1 remains unstable during VX-445 treatment for trapped proteostasis variants.

We performed the same structural modeling and analysis for the VX-445-selective responders (**Supplemental Figure S9, Supplemental Figure S10**). Simulations suggest VX-445 broadly stabilizes the active conformation while failing to stabilize the inactive conformation (**Supplemental Figure S9A-B, Supplemental Dataset S7**), suggesting NBD dimerization may facilitate correction. All selective responders destabilize ICL4 in the active conformation with VX-445, decreasing the ΔRMSD in ICL4 more than in NBD1 (**Supplemental Figure S9C-F**). The inactive conformation shows similar shifts in ICL4 ΔRMSD compared to NBD1 ΔRMSD (**Supplemental Figure SG-H**). These data suggest the energetic contributions of VX-445 to responders dominate in the active conformation and that VX-445 likely corrects by stabilizing ICL4 over NBD1. This is consistent with our findings that VX-445 fails to stabilize NBD1 in trapped poorly responsive variants.

VI. Stabilizing NBD1 rescues poorly responsive variant trafficking

Finally, we sought to rescue the trafficking of poorly responsive variants. Our structural results prompted us to enhance NBD1 stability with secondary mutations. The modeling data posited that poorly responsive variants lack NBD1 stability despite VX-445 binding. Thus, we hypothesized that NBD1 stabilizing secondary mutations may rescue poorly responsive variants. NBD1 stabilizing mutations introduce favorable intermolecular interactions into important NBD1 loop regions[51]. Many previous studies have demonstrated the stabilizing effects of secondary mutations on CF-causing variants; however, they typically combined multiple secondary mutations, obstructing an unbiased assessment of their individual energetic contributions.

We introduced three NBD1 stabilizing mutations, F494N, I539T, and Q637R, into three poorly responsive variants A559T, R560T, and Y569D. Secondary mutations with distinct localization and stabilization mechanisms were selected throughout NBD1 (**Figure 6A**). F494N was discovered in fish species with increased NBD1 solubility[52], and this mutation stabilizes CFTR via the Q-loop (residues 491-500), a loop involved in ATP binding. I539T was discovered in avian species with a higher body temperature (>40 °C) than humans and more stable CFTR. I539T stabilizes the structurally diverse region (SDR – residues 533-548)[53]. Q637R occurs in the helix 8-helix 9 (H8-H9) loop of the NBD1 C-terminus and allosterically stabilizes the ICL4 binding pocket near F508[54].

As a control, we introduced F494N, I539T, and Q637R into F508del and measured drug response. Using a western blot band shift trafficking assay, we found dual drug treatment, and I539T rescued F508del CFTR, while F494N and Q637R rescued only in combination with correctors (**Figure 6B**). I539T plus dual correctors showed the most robust increase in trafficking efficiency.

Secondary mutations rescued A559T despite its trapped proteostasis state during correction. A559T trafficking was rescued by combining drug treatment with F494N and I539T (**Figure 6C**), transforming a poor-

responder into a responder. Productive proteostasis state variants R560T and Y569D both demonstrated trafficking rescue with dual drug treatment in combination with I539T (**Figure 6D-E**). This is consistent with the notion that I539T offers the greatest contribution to ΔT_m of any secondary mutations (~-2.5°C)[43,45]. These results suggest that either 1) energetic contributions comparable to I539T are necessary to rescue poor responders or 2) stabilizing proximate regions such as the Q-loop and SDR specifically may be important for poorly responsive variants in the NBD1 core.

We conclude that poorly responsive variants are not inherently uncorrectable, as evident from the subtly altered proteostasis landscapes and the small degree of structural stabilization observed. However, the current VX-661/VX-445 dual corrector regiment fails to add enough favorable energetic interactions to NBD1. For the first time, we show that poor responders may be rescued by NBD1 stabilizing secondary mutation I539T. This suggests a path forward by which new corrector treatments, perhaps targeting NBD1 directly, may be leveraged to treat poorly responsive CF patients harboring these variants.

DISCUSSION

Despite the advent of revolutionary corrector compounds for treating CF, 10% of persons with CF have no etiological treatment options, with ~3% harboring class II misprocessing variants amenable to correction[4]. Correctors reintroduce intermolecular interactions that CFTR variants lack and consequently rescue the derailed protein homeostasis and structural stability of CFTR. Diverse corrector mechanisms split response profiles into selectively responsive and poorly responsive variants. Until recently, poorly responsive variants have been underrepresented in biochemical studies, although a few exceptions are highlighted below. Poor responders show low allele numbers amongst persons with CF, partially due to their prevalence in underrepresented populations. Increasing access to genetic sequencing among underrepresented persons may reveal additional, emerging poorly responsive variants – creating the need to predict response[55]. Here, we sought to understand the proteostatic and structural deficiencies of selectively responsive and poorly responsive variants to reveal opportunities for correction.

Previous studies have focused little on poorly responsive variants due to under-sampled patient demographics. For example, A559T is common amongst individuals of African descent[56] and is the second most common mutation (after F508del) in the Dominican Republic[57]. R1066C is the second most common variant (after F508del) in Puerto Rican patients[57]. Despite low allele frequency, a few previous *in vitro* studies have characterized poorly responsive variants with correctors in various CF model systems. In stably expressing CF bronchial epithelial cells (CFBEs), variants L558S, A559E/T, and R560T failed to show any response to VX-661/445 combination treatment[17]. A559T only showed 10% WT function after treatment with VX-661/VX-445 in homozygous-derived rectal organoids[18]. Variants V520F, A559T, and Y569D failed to respond to temperature correction in HEK293T cells[16]. By contrast, in CFBEs, V520F and Y569D responded modestly to VX-661/VX-445 together but not VX-661 alone, whereas R560T failed to respond regardless of treatment combination[9]. Stabilizing secondary mutations have also been leveraged to rescue poor responders; for example, G550E, which alters NBD1 conformation, rescues A561E but not R560T[19]. However, few previous studies have compared poorly responsive to responsive variants in the same investigation.

Prior work showed that Type-I corrector VX-809 and Type-III corrector VX-445 attenuated proteostasis interactions across pathways for respective sensitive variants[13,14]. Here, we uncovered that the basal state proteostasis landscapes diverge for selective VX-445 responsive variants – with R1066H showing unique proteostasis interactions during co-translational folding. VX-445 primarily attenuated endocytosis for F508del versus translational proteins for R1066H, showing that different biogenesis stages may be important for correcting different variants. Like VX-809 rescue of F508del[58], VX-445 can rescue responsive CFTR variants at multiple points in the biogenesis pathway, depending on the variant.

Previously, it was postulated that common proteostasis states in the basal condition drove corrector response, e.g. the proteostasis network of selective responders was more amenable to correction than poor responders.[13] Our new results shift this paradigm from a common basal proteostasis state to diverse ones among responsive variants. However, these diverse basal proteostasis states are corrected convergently across pathways. Consequently, VX-445 decreased interactions for all pathways for all responsive variants - indicating that VX-445 rescue primarily involves conferring stability proximate to the mutation site.

VX-809 attenuates F508del interactions with translation, folding, and proteasomal degradation machinery[13]. Unexpectedly, despite better rescue of F508del by VX-445, VX-445 failed to alter F508del proteostasis interactions at any point during biogenesis (**Figure 3C**). The disparity between VX-809 and VX-445 remodeling of the F508del proteostasis landscape lends to the notion that VX-809 acts co-translationally early in biogenesis[6] while VX-445 may act later in the final assembly for F508del. Interestingly, VX-661 and VX-445 together attenuated early biogenesis pathway interactions with translation, folding, and proteasomal degradation (as observed in VX-809) – but additionally attenuated autophagy and lysosomal degradation. This implies either 1) VX-661 adds stability beyond VX-809, despite a shared binding pocket, or 2) that VX-445 added stability prevents alternate degradation via autophagy and the lysosome. We speculate the addition of VX-445 decreases endocytosis-mediated degradation, which preferentially occurs through lysosomal degradation.

Unlike in responsive variants, correctors failed to attenuate interactions across pathways in poorly responsive variants. However, we revealed subtle, albeit important, changes in select pathways for a subset of

variants. V520F, R560T, Y569D, and R1066C CFTR exhibit remodeling of early-stage proteostasis such as translation, folding, and degradation pathways when treated with VX-661 and VX-445 – suggesting drugs guided these variants to productive proteostasis states. Interestingly, V520F and R560T, like F508del, are correctable by temperature reduction (**Figure 1F**). Despite their similarities, corrector treatment attenuates V520F interactions with autophagy versus attenuating R560T and Y569D interactions with proteasomal degradation, suggesting R560T and Y569D structural defects occur early while CFTR is still amenable to retro-translocation.

Other studies have performed FoldX simulations on poorly responsive variants A559T, R560T, and L558S with and without VX-661 and showed the failure of Type-I correctors to stabilize these variants[17]. We further demonstrated that VX-445 fails to stabilize L558S, A559T, and A561E. We hypothesized that enhanced NBD1 stabilization could rescue poorly responsive variants. In combination with dual correction treatment, SDR stabilizing I539T consistently rescued poor responders. However, it remains unclear if I539T energetic contributions (on the order of -2.5°C ΔT_m[43,45]) or location in the SDR is more important for rescuing NBD1 core variants. Regardless, our results suggest NBD1 poorly responsive CFTR variants will likely require NBD1 targeting correctors.

In addition to the poorly responsive variants studied here, many other poorly responsive variants surfaced throughout the CFTR sequence that remain unapproved by the FDA for treatment with VX-445/VX-661 (in combination with VX-770 potentiator) (**Figure 1E**)[20]. These poorly responsive, unapproved variants occur in the TMD1 N-terminus, NBD1, the middle of TMD2, and NBD2. Thus, future work may investigate the proteostatic and structural deficiencies of these poor responders. For NBD1 poorly responsive variants, the I539T secondary mutation rescue results highlight a structural region potentially targetable for virtual drug screening. Alternatively, NBD1 correctors already in development[59] or next-generation correctors[60] may be used to treat NBD1 poor responders characterized here.

We note some important limitations of our study. The expression of different proteostasis components can vary between cell lines and tissue types. However, the CFTR proteostasis network is highly conserved at the pathway level e.g. proteasomal proteins and autophagy proteins between HEK293T cells and other more patient-relevant CF model systems. Thus, we assume our pathway-level analysis of responsive and poorly responsive variants will hold across model systems. Furthermore, the response of CFTR variants between HEK293T cells and CFBEs has been shown to correlate[16], and we observed a consistent response profile for the variants of interest in our system (**Figure 1G-H**). We have also previously shown that interactors identified in HEK293T cells and then knocked down in CFBE cells sensitized P67L to VX-445[14], highlighting the functional conservation of proteostasis factors across cell lines. Our computational modeling is limited to sampling conformational space far from the folding equilibrium process. We note some variants may never reach such folded conformations, as they could be degraded or engaged by chaperones *in vivo*. However, temperature and pharmacological correction indicate misfolding-prone CFTR variants sample near folded conformations in cells under such conditions, although they may comprise a small fraction of the conformational ensemble.

The lack of proper sampling of persons with CF worldwide limits our understanding of the true allelic frequency of poorly responsive variants. Changing patient demographics and the decreasing price of genetic sequencing may change the distributions of alleles in the CF population. This will require efficient assessment strategies for variant responses to current and future correctors to expand treatment to all persons with CF. Overall, we show that proteostasis profiling and computational structural modeling provide a framework for discerning elusive drug response mechanisms. Subtle differences in proteostasis landscape changes among poor responders were accompanied by underlying structural defects among the same variants. This approach may be leveraged by future investigations seeking to expand therapeutics to new or unapproved variants associated with other protein misfolding diseases in broad personalized medicine applications.

METHODS

Bioinformatic analysis

For the analysis of McKee et al., the Deep Mutational Scan (DMS) dataset was downloaded from[10]– specifically Supplementary Table S1. The cell surface immunostaining intensity was normalized to stably expressing WT CFTR HEK293T cells (1695 units). The basal state DMSO vehicle and drug response VX-445 and VX-661 data was split to plot the corrector response as a function of CFTR sequence position. The variants from the DMS study were filtered against an FDA-approved variant list from Vertex Pharmaceuticals[3] (https://www.trikafta.com/who-trikafta-is-for, accessed on 08/2023). Finally, any variants demonstrating >100% WT immunostaining intensity under dual drug treatment were filtered out to only consider poorly responsive variants that are not FDA-approved. For the analysis of the Bihler et al. dataset, the Supplementary Table S1 dataset was downloaded from[20]. Then, missense variants were included and filtered against the FDA-approved variants list based on the website above. Next, DMSO and VX-445/661 treated conditions were split, and only trafficking data was considered to look at misfolding and mis-trafficking (not gating mutations) to focus on variants that would be amenable to correctors. Variants with <25% WT C/(C+B) band ratio under dual drug treatment conditions were considered poorly responsive and plotted. The basal condition and drug condition for each variant were plotted as a function of the CFTR sequence. Finally, for reanalysis of the Anglés et al. data set, it was downloaded from[16] and filtered against the FDA-approved variants. Again, trafficking data was used to discover temperature correction insensitive variants that may be amenable to correction. The standard temperature trafficking index (TrIdx 37) and the reduced temperature corrected trafficking index (TrIdx 27) were plotted for each variant as a function of the CFTR sequence and connected with a line. Variants with >90% WT temperature correction were removed to focus on non-temperature responsive variants. Then, clusters of poorly responsive and selectively responsive variants were mapped onto the CFTR structure to reveal overlap (**Figure 1**).

Plasmids and antibodies

CFTR expression plasmids in the pcDNA5 vector were gifted from E. Sorscher and J. Hong (Emory University, Atlanta, Georgia)[61]. Site-directed mutagenesis with Q5 polymerase (New England BioLabs) was used to introduce selectively VX-445 responsive (L165S, Y1032C, T1036N, H1054D, and R1066H) and poorly responsive mutations (V520F, L558S, A559T, R560T, A561E, Y569D, and R1066C) in WT CFTR expression vectors. KLD enzyme reaction (New England BioLabs) was used to ligate the PCR product and digest the WT template. All plasmids were confirmed by Sanger sequencing of the local region (Azenta).

CFTR immune blotting was performed with anti-CFTR 217 R-domain mouse monoclonal antibodies (http://cftrantibodies.web.unc.edu/) that were purchased from J. Riordan (University of North Carolina, Chapel Hill, North Carolina – The Cystic Fibrosis Molecular/Functional Measurement Core). CFTR co-immunoprecipitation was performed with 24-1 anti–C-terminus monoclonal antibodies (ATCC HB-11947), which were purified by Protein-G affinity chromatography on an ÄKTA Start protein purification system (GE Life Science) from B lymphocyte hybridoma cell culture medium. Ab was covalently conjugated to Recombinant Protein G - Sepharose 4B (6 mg antibody per mL of beads). Antibodies were used in immunoblotting buffer (5% bovine serum albumin [BSA] in Tris-buffered saline, pH 7.5, 0.1% Tween-20, and 0.1% NaN_3) at 1:1000 dilutions of each primary antibody. Fluorescent secondary antibodies were purchased and used at the indicated dilutions in 5% milk in Tris-buffered saline (TBS), 0.1% Tween-20 (TBS-T): goat anti-mouse Starbright700 (1:10,000, Bio-Rad), anti-rabbit rhodamine-conjugated tubulin (1:10,000, Bio-Rad). Immunoblotted PVDF membranes were rinsed three times for 10 minutes in TBS-T and incubated with secondary antibodies in 5% milk at room temperature for 30 minutes. Following an additional three TBST washes for five minutes each, membranes were imaged for CFTR using a ChemiDoc MP Imaging System (BioRad).

Cell culture, immunoprecipitation, SDS–PAGE, and immunoblotting

HEK293T cells were maintained in Dulbecco's Modified Eagle's Medium of high glucose with 10% fetal bovine serum, 1% penicillin/streptomycin, and 1% glutamine. Cells were transiently transfected 24 hours after seeding 2 × 10^5 cells/mL with CFTR expression plasmids of respective variants using the calcium phosphate method[62]. At 16-18 hours post-transfection, cell growth media was replaced and treated with either DMSO vehicle, 3 μM VX-445 for the selectively responsive variants, or 3 μM VX-445 + 3 μM VX-661 for the poorly responsive variants. Approximately 24 hours after treating cells, a 10cm plate with fully confluent cells (approximately 10^7 cells) was collected for each experimental condition. Cells were lysed and harvested directly from the plate by first rinsing in phosphate-buffered saline (PBS) and then incubating in TN buffer with 0.5% IGEPAL CA-630 and a Mini, EDTA-free Protease Inhibitor Cocktail (Roche) cocktail at 4 °C for 20 minutes. Subsequently, cells were dislodged using a cell scraper, sonicated for 3 minutes, and centrifuged at 18,000 g for 15-30 minutes. Total protein concentration was normalized using a Pierce BCA Protein Assay kit (Thermo Scientific).

A sample of each lysate, i.e.., input fraction, was collected and denatured with 6X Laemmli buffer + 100 mM DTT and heated at 37°C for 15 minutes. SDS-PAGE on 8% acrylamide gel was employed for separation, followed by transfer onto PVDF membranes for immunoblotting as outlined above.

Co-immunoprecipitation protein identification technology (CoPIT), developed by Pankow et al., was utilized for the direct affinity purification of CFTR and its interacting proteins, as previously outlined[63]. In brief, for immunoprecipitation, cell lysates underwent pre-clearance with 100 μL 4B Sepharose beads (Sigma) at 4°C for 1 hour while rocking. Subsequently, the precleared lysates were subjected to immunoprecipitation using 100 μL slurry (50% beads/50% buffer) Protein G sepharose beads covalently conjugated to 24-1 anti-CFTR mAB (6 mg antibody per mL of beads) overnight at 4°C while rocking. The following day, a portion of the supernatant was collected, e.g., a clear fraction representing residual proteins not captured by the beads, for Western blot analysis. Beads and interacting proteins were washed thrice with TNI buffer to remove any non-specific interactors and twice with TN buffer to remove IGEPAL detergent. Then, beads were frozen at -80 °C for at least 1.5 hours or overnight. Interacting proteins were eluted from beads twice while shaking at >700 rpm at 37 °C for 30 minutes to 1 hour using a 0.2 M Glycine (pH 2.3), 0.5% IGEPAL CA-630 buffer. A portion of the elution, e.g., elution fraction, was collected and run on SDS-PAGE and immunoblotted as described previously to determine immunoprecipitation and elution efficiency. The remainder of the elution was prepared for mass spectrometry analysis.

Multiplexed LC-MS/MS

Sample preparation for multiplexed LC-MS/MS was performed as previously described[13,14]. Digested peptide samples were TMT-labeled with TMT Pro 16-plex reagents or 18-plex reagents (Thermo Fisher) in 40% v/v acetonitrile for one hour at room temperature (**Supplementary Table 1**). LC-MS/MS analysis was performed using an Exploris 480 (Thermo Fisher) mass spectrometer equipped with an UltiMate3000 RSLCnano System (Thermo Fisher). MudPIT experiments were performed with eight 10 μL sequential injections of 0, 10, 20, 40, 60, 80, and 100% buffer C (500 mM ammonium acetate in buffer A), followed by a final injection of 90% buffer C with 10% buffer B (99.9% acetonitrile, 0.1% formic acid v/v). Each injection step was followed by a 6 minute 2% B to 2 minute 2% - 5% B, 92-minute gradient from 5% to 35% B , followed by a 5-minute gradient from 35%-65% B, and 1 minute 65% - 85%, held for 7 minutes to drop to 2% instantly and held for 17 minutes for a total of 130 minutes at a flow rate of 500 nL/min, on a 20 cm fused silica microcapillary column (ID 100 μM) ending with a laser-pulled tip filled with Aqua C18, 3 μm, 100Å resin (Phenomenex).

Electrospray ionization (ESI) was performed directly from the tip of the column, applying a voltage of 2.2 kV and an ion transfer tube temperature of 275°C. Data-dependent acquisition of MS/MS spectra was performed by scanning from 375-1500 m/z with a resolution of 120,000. Peptides with an intensity above 5.0E3 with charge state 2-7 from each full scan were fragmented by high collision dissociation with pure N_2 gas using normalized collision energy of 36, with a 0.7 m/z isolation window, 150 ms maximum injection time, at a

resolution of 45,000 scanned at a defined first mass at 110 m/z and dynamic exclusion set to 45, and a mass tolerance of 10 ppm. MS data is available for VX-445 selective responsive variants (**Supplemental Dataset S8**) and poorly responsive variants (**Supplemental Dataset S9**).

Interactome characterization

Peptide identification and protein quantification based on TMT label relative abundance were conducted using Proteome Discoverer 2.4. MS/MS spectra were extracted from Thermo XCaliber .raw file format and subjected to Sequest HT search against a Homo sapiens database (SwissProt TaxID=9606) comprising 42,252 protein entries. Searches utilized a decoy database of reversed peptide sequences, employing the following parameters: 10 ppm peptide precursor tolerance, 0.02 Da fragment mass tolerance, a minimum peptide length of 6 amino acids, trypsin cleavage allowing a maximum of two missed cleavages, static cysteine modification of 57.0215 (carbamidomethylation), and static N-terminal and lysine modifications of 304.207 (TMT 16plex or 18plex). SEQUEST search outcomes were filtered through Percolator to limit the peptide false discovery rate to 1%, requiring a minimum of two unique peptides for each protein identification. TMT reporter ion intensities were quantified using the Reporter Ion Quantification processing node in Proteome Discoverer 2.4 and summed for peptides associated with the same protein.

To identify interactors, we used median normalized TMT intensity to compare experimental conditions to mock transfection control. We assume that most identified proteins are nonspecific interactors present in similar amounts in both the mock and CFTR-bait Co-IP samples. Median normalization decreases TMT intensity variability across different LC-MS/MS runs and allows data aggregation between runs (**Supplemental Figure S2A-B and S4A-B**).

Statistical analysis

To determine statistically significant CFTR interactors, we used a two-tailed paired t-test with scipy.stats.ttest_rel (https://docs.scipy.org/doc/scipy/) package in Python to calculate the p-value between the log2 TMT intensity of each protein over the corresponding log2 TMT intensity in the mock-transfected control condition. A volcano plot with a hyperbolic curve $y > c/(x - x0)$, where y is the adjusted p-value, x is the log2 fold change, x0 is the standard deviation (0.5σ or 1σ), and c is the curvature ($c = 0.4$). We considered proteins greater than the 1σ curve high confidence interactors and proteins greater than the 0.5σ curve to be medium confidence interactors.

For the distribution of interactors depicted as violin plots in Figures 3 and 4, a one-way ANOVA with Geisser-Greenhouse correction and Tukey post-hoc multi-hypothesis correction was used to determine statistical significance. For these statistical calculations, adjusted *p*-values were depicted by *< 0.05, **< 0.01, ***< 0.001, and ****< 0.0001. For RosettaCM-based simulation and calculations, a non-parametric Wilcoxon test was used to determine statistical significance from zero. For western blots, a parametric ratio-paired t-test was used. For these statistical calculations, p-values are depicted by * < 0.05, **< 0.01, *** < 0.001, and **** < 0.0001.

Pathway analysis

We manually annotated pathways by cross-referencing gene names on UniProt and classifying pathways using Gene Ontology (GO) terms related to Biological Pathway as previously described[13]. Pathway assignments in the selectively responsive and poorly responsive datasets were cross-referenced to ensure consistent assignment of putative pathways in both datasets.

CFTR Rosetta Comparative Modeling

We modeled CFTR mutants using previously established Rosetta Comparative Modeling (CM) methods[43]. Briefly, 2000 model ensembles of inactive and active CFTR conformations (PDB ID 5UAK[49] and 6MSM[48]m, respectively) were refined using automated refinement into the cryo-EM density map with Rosetta[50]. The lowest-

scoring five models were selected for docking of VX-445 because cryo-EM refinement contains different coordinates than the published VX-445 bound models. Quantitative comparison between the apo and VX-445 bound mutant models requires initializing RosettaCM from the same starting coordinates. Conformational ensembles of VX-445 were generated with the BCL ConformerGenerator[64] and exported Rosetta-readable parameter file for ligand docking. To dock VX-445, we aligned BCL parameterized VX-445 to the same coordinates as the published bound models[8] in Chimera and saved the aligned corrector coordinates.

VX-445 was docked 1000 times using full atom docking simulations with RosettaLigand[65] for 24 cycles, repacking every cycle. The interface energy scores and non-superimposed root mean squared (rms) deviation from aligned published VX-445 bound models (PDB ID 8EIQ)[8] were reported. We chose the docked pose with the least squared distance from the lowest scoring model and rms from the published model as a final template for *in silico* mutagenesis.

Point mutations were introduced using the MutateResidue mover in Rosetta. The active state model, 6MSM[48], was mutated back to E1371 (naturally occurring glutamine residue) before refinement. Following VX-445 docking, we mutated patient mutations into the cryo-EM refined template models. F508del was modeled as previously by deleting F508 from the CFTR fasta sequence and threading the sequence onto docked template models. Finally, RosettaCM[66] was performed using five mutated templates in the apo or VX-445 bound state. We used RosettaCM with multiple template hybridization using the HybridizeMover guided by the RosettaMembrane energy function[67,68] with membrane-specific Rosetta energy terms imposed by a theoretical membrane bilayer defined by the transmembrane helix regions with the OCTOPUS prediction software[69].

RosettaCM Analysis

We assessed the thermodynamic stability of CFTR variants using the Rosetta score and the alpha carbon (Ca) root mean squared deviation (RMSD). We calculated the change energy by subtracting the average Rosetta energy score of the apo ensemble from that of the WT ensemble. Additionally, we determined the energy change for VX-445 binding by subtracting the average Rosetta energy score of the VX-445 bound ensemble from that of the apo ensemble. RMSD was calculated per residue in reference to the lowest-scoring model in the ensemble as previously described[43].

Comparison of variant instability and VX-445 induced stability. ΔRMSD between apo variant and WT CFTR in was mapped onto the corresponding CFTR structure from which the models were derived (e.g., active or inactive). The ΔRMSD for NBD1 (residues 485-572) were quantified because they contact TMD2 via ICL4. Mutation instability was calculated by the ensemble RMSD of variant versus WT CFTR (**Figure 5C**). Likewise, VX-445 stability was calculated by the ensemble RMSD by residue is shown for VX-445 bound variant and apo variant CFTR (**Figure 5C**). The summed ΔRMSD values were presented as bar plots.

ACKNOWLEDGEMENTS

This work was supported by R35 GM133552 (NIGMS) and R01 HL167046 (NHBLI). EFM was supported by a predoctoral fellowship F31 HL162483 (NHLBI) and Chemical-Biology Interface training grant T32 GM065086 (NIGMS). We thank Olivia Paige Black for helping with the material preparation and Asaf Elazar for helpful feedback on the figures.

AUTHOR CONTRIBUTIONS

Conceptualization: E.F.M., L.P.; Funding acquisition: E.F.M., L.P., J.M.; Experimental Design: E.F.M., L.P.; Experimental Data Collection: E.F.M., M.K., J.O.; Computational Design: E.F.M., J.M.; Computational Data Collection: E.F.M.; Data Analysis: E.F.M.; Writing original draft: E.F.M.; Writing review and editing, E.F.M., M.K., J.O., J.M., L.P. All authors have read and agreed to the published version of the manuscript.

FIGURES

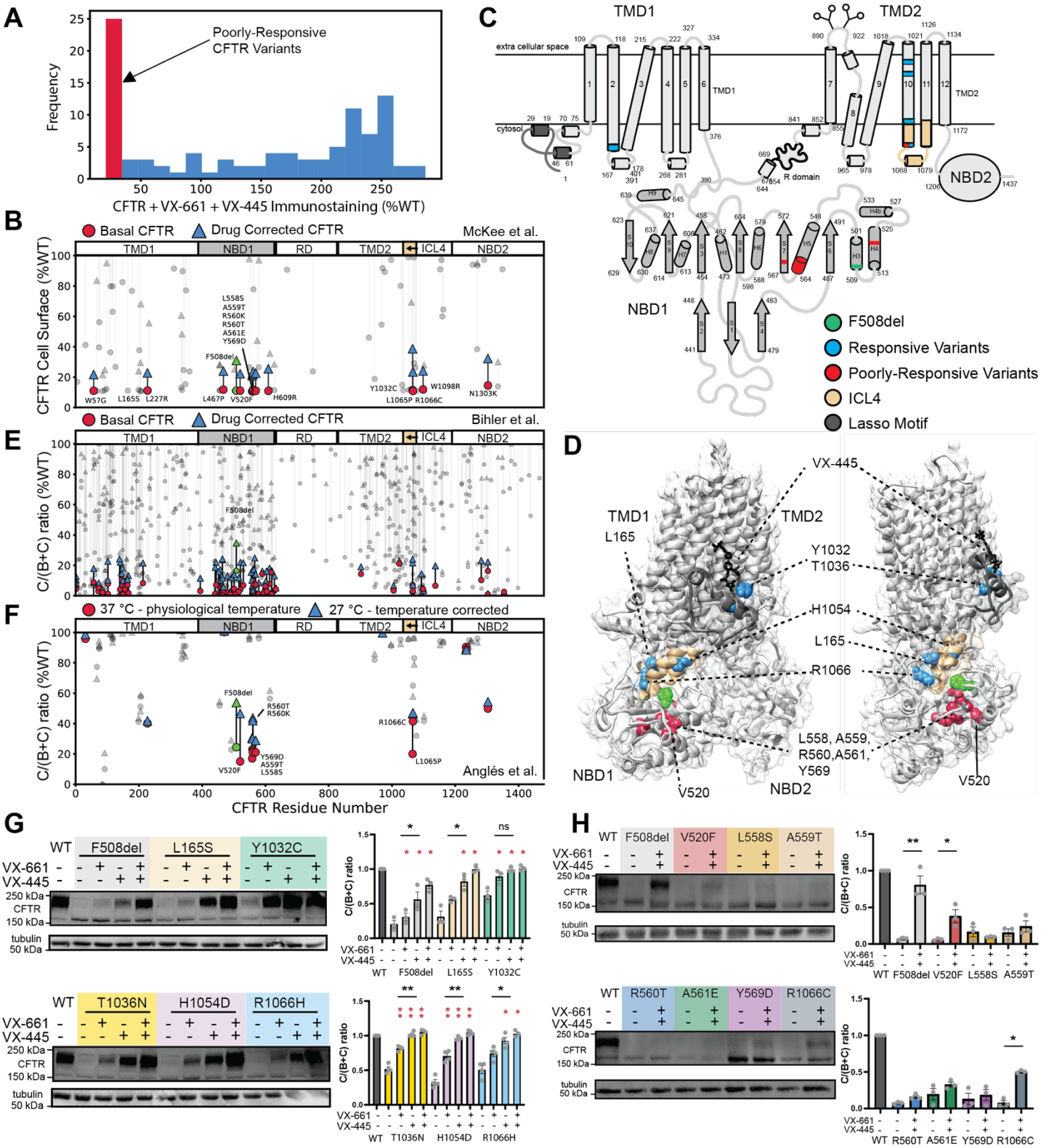

Figure 1. Identification and location of VX-445 selectively responsive and poorly responsive CFTR variants.

A. Histogram of CFTR cell surface immunostaining intensity in percent WT (%WT) under VX-661 and VX-445 dual treatment conditions reveals variants that fail to respond to correctors[10].

B. CFTR cell surface immunostaining as assessed by deep mutational scanning (DMS) from[10]. CFTR residues are resolved by sequence position on the x-axis. Cell surface staining intensity on the y-axis is expressed as percent WT (%WT) for basal (red circles) and dual corrector (VX-661 and VX-445) treatment (blue triangle) conditions. The black line connecting each variant basal level to the drug level represents the magnitude of drug response. For reference, approved variants are shown in grey. Variants with >100% WT drug response were removed for clarity. Unapproved, poorly responsive CFTR mutations cluster in the alpha-helical subdomain of NBD1 (residues 460-600) and inter-cellular loop4 (residues 1030-1080).
C. Ribbon diagram of the CFTR membrane topology and NBD1 structure with VX-445 selectively responsive variants highlighted in blue and poorly responsive variants highlighted in red. F508 is shown in green, ICL4 is shown in tan, and the lasso motif is shown in dark grey for reference.
D. CFTR inactive state cryo-EM model (PDB ID 5UAK)[49] demonstrates VX-445 selectively responsive and poorly responsive variants both cluster in the three-dimensional structure at the ICL4/NBD1 core binding interface. Colored the same as **C.**
E. Reanalysis of CFTR trafficking data versus from[20]. Variants are resolved based on sequence position on the x-axis. The y-axis shows the measured C/B band ratio in percent WT (%WT) under basal (red circle) and dual corrector (VX-661 and VX-445) treatment (blue triangle) conditions. Approved variants are shown in grey. Variants with >25% WT drug response were removed for clarity.
F. Reanalysis of CFTR trafficking data versus sequence position from[16]. The Y-axis shows measured C/(C+B) band ratio representing the trafficking efficiency in percent WT (%WT) under standard temperature (37 C – red circles) and reduced temperature (27 C – blue triangles) conditions with a black line representing drug response magnitude. FDA-approved variants were filtered out and are shown in grey. The remaining variants reveal the temperature correction profiles of unapproved variants.
G. Representative Western blots depicting VX-445 selectively responsive variants L165S, Y1032C, T1036N, H1054D, and R1066H CFTR under basal, VX-661, VX-445, and dual drug treatment conditions. WT and F508del CFTR are shown as controls. Quantification shows all variants demonstrate an increased trafficking efficiency as measured by the C/(C+B) band ratio in response to VX-445 (red asterisks). Additionally, all variants but Y1032C show a response difference between VX-445 and VX-661 (black asterisks), indicating these variants are indeed VX-445 selectively responsive in the transient HEK293T cell system.
H. Western blots depicting poorly responsive variants V520F, L558S, A559T, R560T, A561E, Y569D, and R1066C CFTR under basal versus VX-661 + VX-445 dual treatment conditions. WT and F508del CFTR are shown as controls. The lack of maturely glycosylated C band CFTR during dual drug treatment indicates these variants are indeed poorly responsive in the transient HEK293T cell system. Statistical significance was calculated using a parametric ratio paired t-test, and p values are depicted by *< 0.05, **< 0.01, ***< 0.001, and ****< 0.0001.

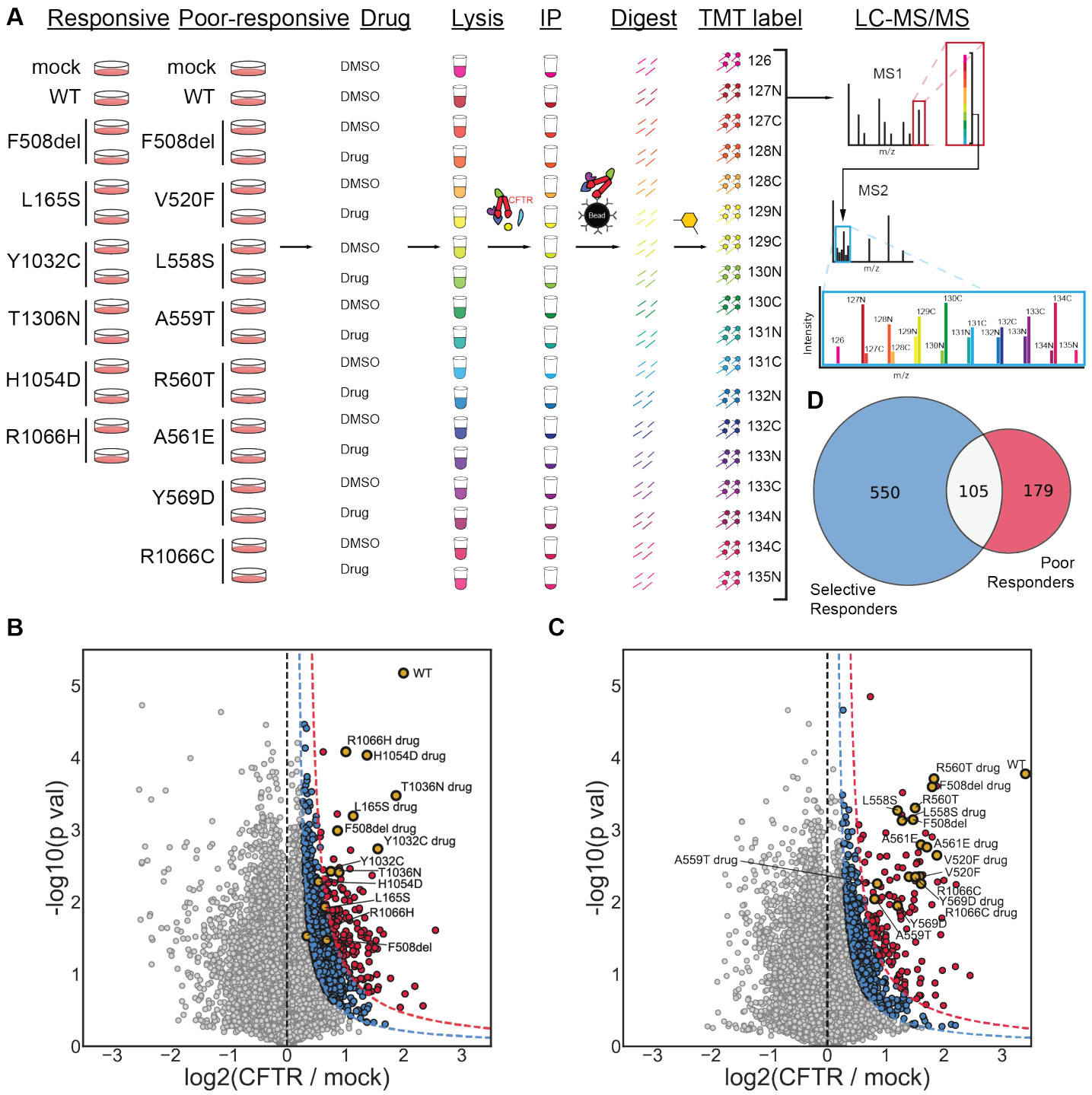

Figure 2. Quantitative interactomics of VX-445 selectively responsive and poorly responsive variants.
A. Quantitative affinity purification mass spectrometry interactomics workflow for identifying CFTR interactors. HEK293T cells are transiently transfected with CFTR variants of interest in a set of either VX-445 selective responders or a set of poorly responsive variants. Cells are then drug-treated with CFTR correctors, lysed, collected, and normalized. CFTR interactors are immunoprecipitated, eluted, and digested into their component peptides, which are labeled with isobaric TMT labels for multiplexed mass spectrometry analysis and quantification.
B. Volcano plot of VX-445 selective responder interactors. Interactors were identified using a curved cutoff at 0.5σ for medium confidence (blue) and 1σ for high confidence (red) proteins. CFTR, shown in gold, of each variant was enriched across conditions. Interacting proteins across selectively responsive variant were added to a

master list comprising 655 interactors for this data set (see **Supplemental Figure S2 and S3** for individual variant volcano plots).

C. Volcano plot of poorly responsive interactors identified using a curved cutoff at 0.5σ for medium confidence (blue) and 1σ for high confidence (red) proteins. CFTR, shown in gold, of each variant was enriched for all mutants with and without drug treatment. Interacting proteins across poorly responsive variants were added to a master list comprising 284 interactors for this data set (see **Supplemental Figure S4 and S5** for individual variant volcano plots).

D. Overlap of 105 shared interactors between the 655 interactors identified in the VX-445 selectively responsive dataset and 284 interactors identified in the poor-responder dataset.

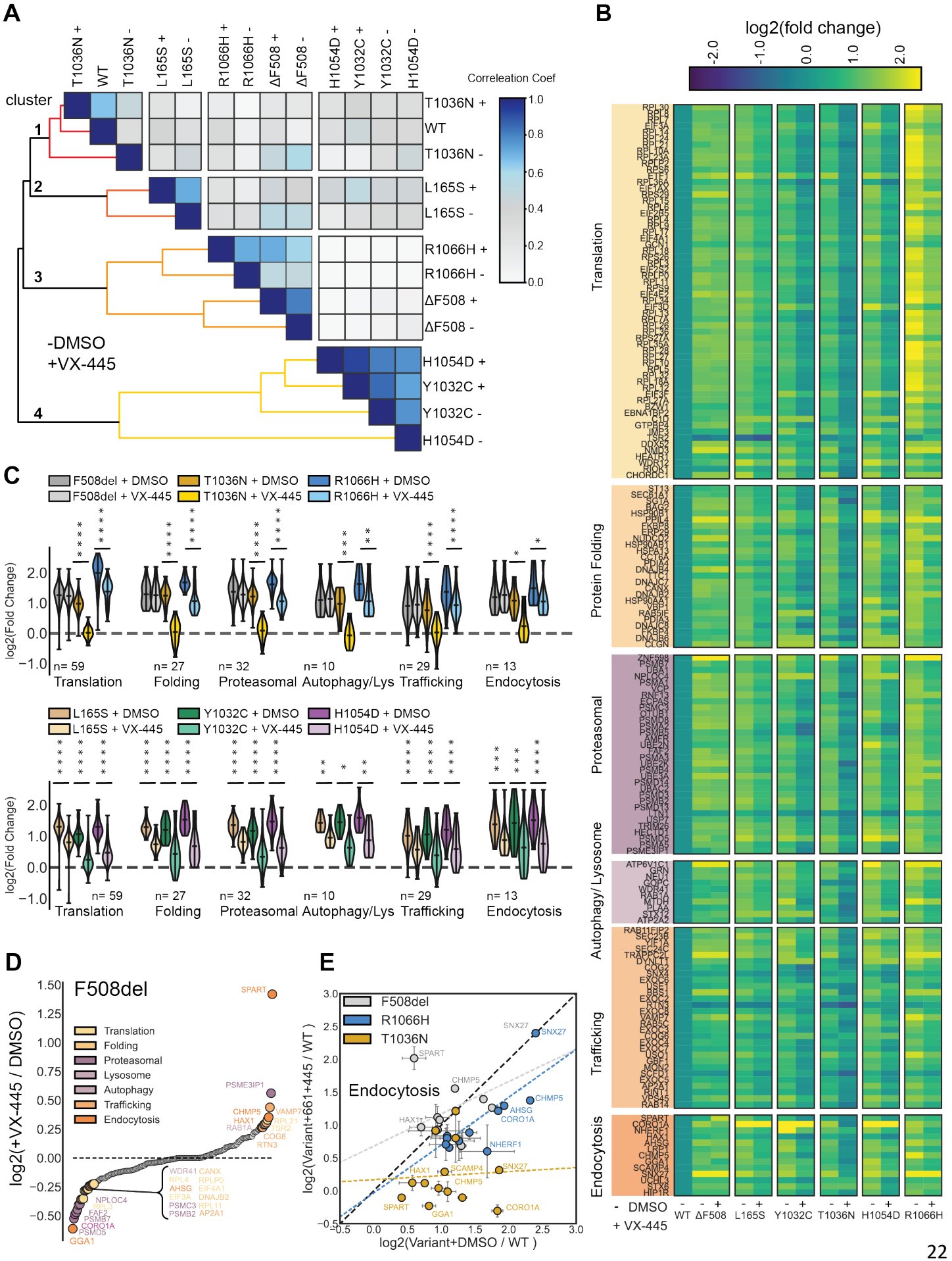
A
T1036N +
WT
T1036N -
L165S +
L165S -
R1066H +
R1066H -
ΔF508 +
ΔF508 -
H1054D +
Y1032C +
Y1032C -
H1054D -
cluster
1
2
3
4
-DMSO
+VX-445
Correleation Coef
B
log2(fold change)
Translation
Protein Folding
Proteasomal
Autophagy/ Lysosome
Trafficking
Endocytosis
- DMSO
+ VX-445
WT ΔF508 L165S Y1032C T1036N H1054D R1066H
C
F508del + DMSO
F508del + VX-445
T1036N + DMSO
T1036N + VX-445
R1066H + DMSO
R1066H + VX-445
L165S + DMSO
L165S + VX-445
Y1032C + DMSO
Y1032C + VX-445
H1054D + DMSO
H1054D + VX-445
log2(Fold Change)
n= 59
n= 27
n= 32
n= 10
n= 29
n= 13
Translation
Folding
Proteasomal
Autophagy/Lys
Trafficking
Endocytosis
D
F508del
log2(+VX-445 / DMSO)
Translation
Folding
Proteasomal
Lysosome
Autophagy
Trafficking
Endocytosis
SPART
PSME3IP1
CHMP5
HAX1
VAMP7
RAB1A
RPL21
TSR2
COG6
RTN3
WDR41
CANX
RPL4
RPLP0
AHSG
EIF4A1
EIF3A
DNAJB2
PSMC3
RPL11
PSMB2
AP2A1
NPLOC4
RPL5
FAF2
PSMB7
CORO1A
PSMD5
GGA1
E
F508del
R1066H
T1036N
Endocytosis
log2(Variant+661+445 / WT)
log2(Variant+DMSO / WT)
SNX27
SPART
CHMP5
AHSG
CORO1A
HAX1
NHERF1
SCAMP4
GGA1

Figure 3. The proteostasis landscape of VX-445 selectively responsive variants reveals interaction attenuation across pathways.

A. Ranked Spearman correlation coefficient cluster-map of 170 proteostasis interactions correlations between VX-445 selectively responsive variants. Ordered into four clusters by K means clustering. T1036N clusters with WT, L165S clusters independently, F508del clusters with R1066H, and Y1032C clusters with H1054D.

B. Heatmap depicting interactions log2 fold changes of variants normalized to WT CFTR and organized by pathways from GO-term analysis. Yellow represents interactions that are upregulated compared to WT, blue represents interactions that are downregulated compared to WT. These responsive variants demonstrate a remodeling toward WT interactions levels during VX-445 treatment, with Y1032C and T1036N showing some of the strongest remodeling.

C. Violin plots of protein enrichment distribution levels for proteostasis pathways from **B.** with known consequences for CFTR. Side-by-side comparisons under DMSO (vehicle) and VX-445 (3 μM) treatment conditions are shown. F508del, T1036N, and R1066H are shown together due to consistent clustering overlap from interaction correlations. F508del shows little change in proteostasis interactions in the presence of 3 μM VX-445. By contrast, VX-445 reduced T1036N and R1066H interactions for translation, protein folding, proteasomal degradation, autophagy/lysosome protein, trafficking, and endocytosis. Statistical significance was calculated using a one-way ANOVA with Geisser-Greenhouse correction and Tukey post-hoc multi-hypothesis correction, and adjusted p values were depicted by *< 0.05, **< 0.01, ***< 0.001, and ****< 0.0001.-445 reduced all variants interactions for translation, protein folding, proteasomal degradation, autophagy/lysosome protein, trafficking, and endocytosis. Statistical significance calculated identical to **C.**

D. Waterfall plot of the log2 fold change between F508del + 3 μM VX-445 over F508del + DMSO organized by rank order of fold change. Interactors above zero are stronger under drug treatment, and interactors under zero are greater in the basal state. Interactors deviating more than one-half standard deviation from the distribution are colored by pathway. VX-445 treatment enriches endocytosis and trafficking factors, whereas the basal state enriches several proteasomal degradation factors.

E. Correlation of individual endocytosis protein quantification between DMSO and VX-445 treatment for F508del (grey), T1036N (gold), and R1066H (blue). A normal line (black dotted line) represents x = y, i.e. no change with the drug. A least squared linear best fit dotted line colored for each variant represented the off-normal axis behavior for each variant during drug treatment. T1036N shows the greatest off-axis best-fit line, indicating endocytosis interactions are substantially altered during VX-445 treatment.

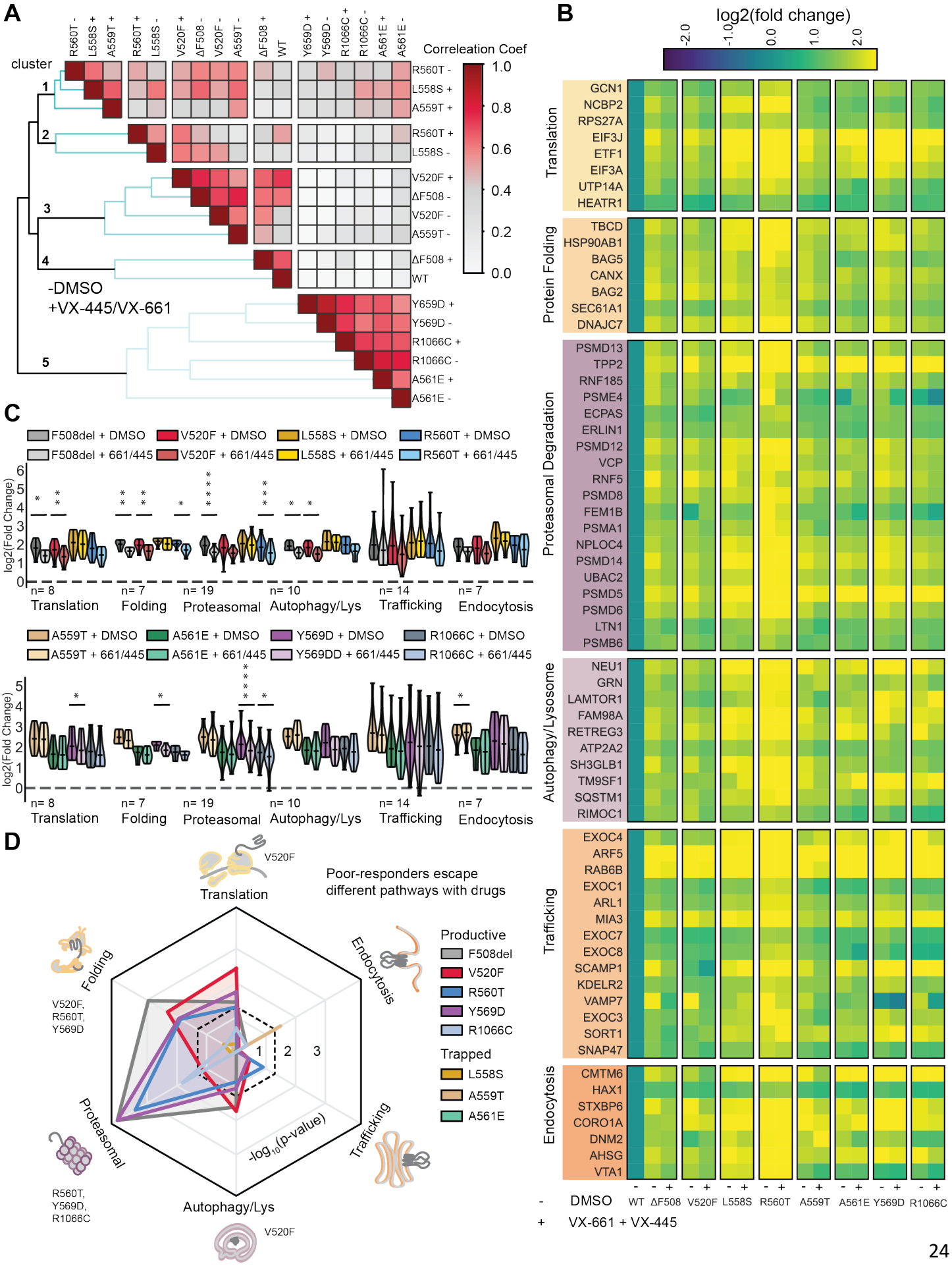
A
cluster
Correleation Coef
-DMSO
+VX-445/VX-661
B
log2(fold change)
Translation
Protein Folding
Proteasomal Degradation
Autophagy/Lysosome
Trafficking
Endocytosis
DMSO
VX-661 + VX-445
C
F508del + DMSO
F508del + 661/445
V520F + DMSO
V520F + 661/445
L558S + DMSO
L558S + 661/445
R560T + DMSO
R560T + 661/445
A559T + DMSO
A559T + 661/445
A561E + DMSO
A561E + 661/445
Y569D + DMSO
Y569DD + 661/445
R1066C + DMSO
R1066C + 661/445
log2(Fold Change)
n= 8 Translation
n= 7 Folding
n= 19 Proteasomal
n= 10 Autophagy/Lys
n= 14 Trafficking
n= 7 Endocytosis
D
Poor-responders escape different pathways with drugs
Translation
Folding
Endocytosis
Proteasomal
Trafficking
Autophagy/Lys
V520F
V520F, R560T, Y569D
R560T, Y569D, R1066C
-log10(p-value)
Productive
F508del
V520F
R560T
Y569D
R1066C
Trapped
L558S
A559T
A561E

Figure 4. Poorly responsive variants diverge into trapped versus productive proteostasis states.
A. Spearman ranked correlation coefficient cluster-map for 65 proteostasis interactions correlated between poorly responsive variants. Ordered into five clusters using K means clustering.
B. Heatmap depicting interactions log2 fold changes of variants normalized to WT CFTR and organized by pathways from GO-term analysis as in **Figure 3**. Yellow represents interactions that are upregulated compared to WT; blue represents interactions that are downregulated. Poorly responsive variants show little difference in interaction levels during VX-445/VX-661 treatment, with V520F showing the most change.
C. Violin plots of protein enrichment distribution levels for proteostasis pathways from **C.** under basal and VX-445/VX-661 (3 μM) treatment. F508del, V520F, L558S, and R560T are shown together due to cluster overlap in **B.** Top: Dual treatment reduced F508del and V520F interactions with translation, protein folding, and autophagy/lysosomal proteins. On the other hand, dual treatment reduced R560T interactions with protein folding and proteasomal degradation machinery only. Dual treatment failed to change interaction levels for L558S, consistent with its kinetically trapped misfolding pathway[70]. Bottom: Violin plots of protein enrichment distribution levels for proteostasis pathways from **C.** under basal and VX-445/VX-661 (3 μM) treatment. A559T, A561E, Y569D, and R1066C are shown together due to cluster overlap in **B**. Dual treatment reduced translation, protein folding, and proteasomal degradation interactions with Y569D as well as proteasomal degradation interactions with R1066C. A559T and A561E interactions remain unaltered by correctors except for a small mean increase in endocytosis for A559T. Statistical significance was calculated using a one-way ANOVA with Geisser-Greenhouse correction and Tukey posthoc multi-hypothesis correction, and adjusted p values were depicted by *< 0.05, **< 0.01, ***< 0.001, and ****< 0.0001.
D. Spider plots depicting the -log10 (p values) from the violin plots in **C.** and **D.** across proteostasis pathways. The black dotted line represents a p-value of 0.05 and serves as a minimum cut-off for statistical significance. V520F shows a distinct pattern with more significant translation and autophagy degradation changes. By contrast, R560T and Y569D show a similar pattern where proteasomal degradation changes are the most significant.

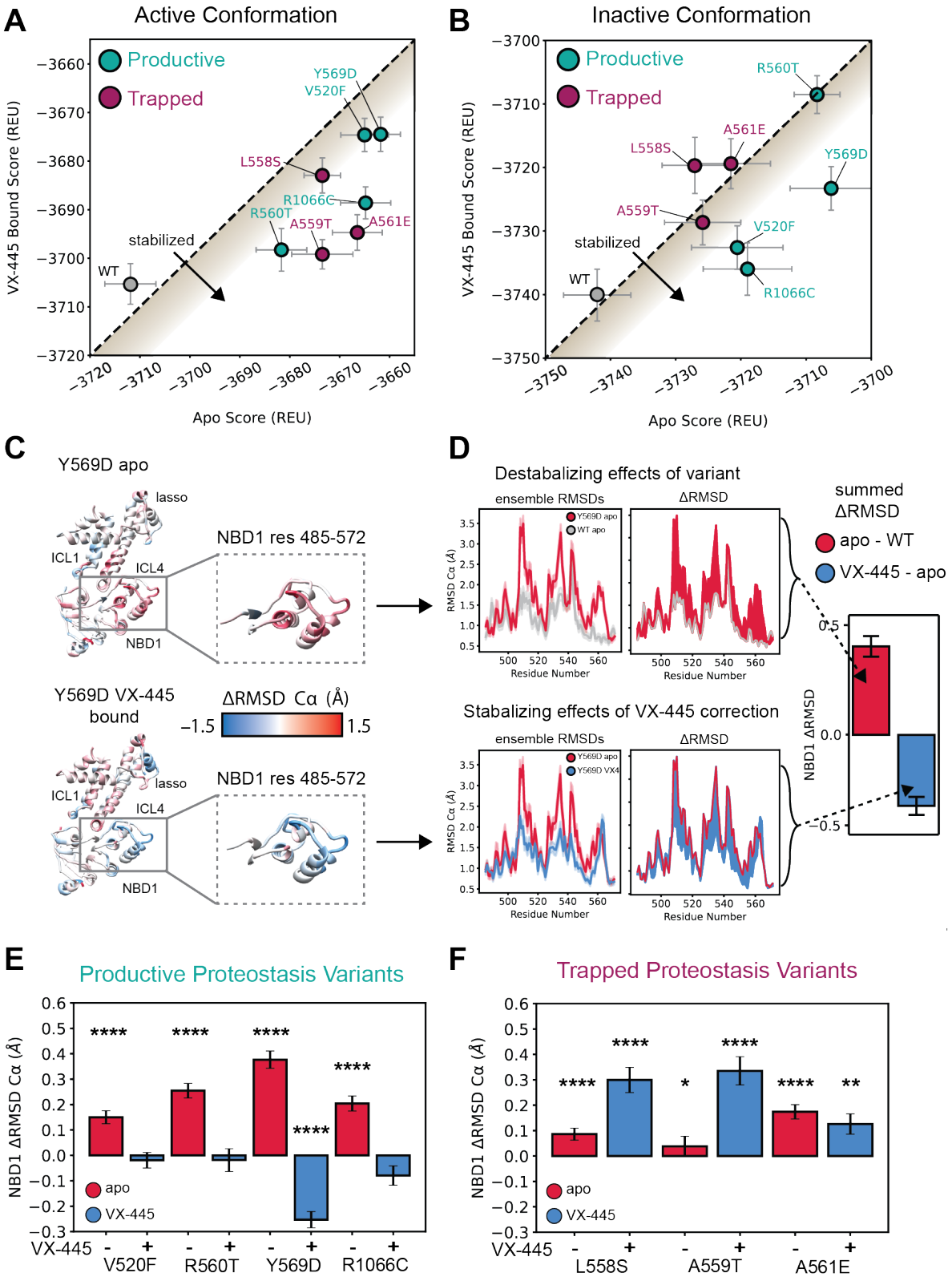

Figure 5. VX-445 fails to stabilize NBD1 of trapped proteostasis poorly responsive variants.
A. The average Rosetta energy scores of the active conformation VX-445-bound state are plotted against the apo state CFTR models for productive proteostasis poor responders (purple) and trapped proteostasis poor responders (gold). A dotted black line with a slope of one intersecting the origin (no effect) is shown for reference. Points represent the average Rosetta energy score, and the error bars represent the standard error of the mean across the

100 lowest (10%) energy-scoring models from an ensemble of 1000 active state models generated for each variant. VX-445 stabilized variants falling below the dotted line. Productive proteostasis variants are shown in green, and trapped proteostasis variants are shown in violet.

B. The average Rosetta energy scores of the inactive conformation VX-445-bound state are plotted against the apo state CFTR models, colored as in **A**. Points represent the average Rosetta energy score, and the error bars represent the standard error of the mean.

C. Comparison of variant instability and VX-445 conferred stability. On top, the ΔRMSD between apo Y569D and WT CFTR in the inactive conformation was mapped onto PDB ID 5UAK[49]. On the bottom, the ΔRMSD between VX-445 bound Y569D and apo Y569D CFTR in the inactive conformation was mapped onto PDB ID 5UAK[49]. Intercellular Loop 1 (ICL1), ICL4, Lasso motif, and NBD1 are shown for clarity. NBD1 ΔRMSD (residues 485-572) were considered because they contact TMD2 via ICL4.

D. Quantification of average ΔRMSD in NBD1 residues 485-572 as an example calculation. On top, the ensemble RMSD by residue is shown for apo Y569D and WT CFTR, followed by a plot showing the ΔRMSD between the RMSDs shaded in red. This represents the instability caused by the Y569D mutation in NBD1. On the bottom, the ensemble RMSD by residue is shown for VX-445 bound Y569D and apo Y569D CFTR, followed by a plot showing the ΔRMSD between the RMSDs shaded in blue. This represents the stability conferred by VX-445 to Y569D NBD1. ΔRMSD values are summed in the quantification bar plot portrayed in **E.-F.** below.

E. Summed ΔRMSD of NBD1 residues 485-572 for poorly responsive variants that showed productive proteostasis states under drug treatment. Quantifications are shown in the inactive conformation. Error bars represent the standard error of the mean and are colored as in **5D.**

F. Summed ΔRMSD of NBD1 residues 485-572 for poorly responsive variants that showed a trapped proteostasis shift under drug treatment. Quantifications are shown in the inactive conformation. Error bars represent the standard error of the mean and are colored as in **4D.** Statistical significances for **E.** and **F.** were calculated using a non-parametric Wilcoxon signed-rank test compared to zero to determine if distributions were significantly different from zero, and p values were depicted by *< 0.05, **< 0.01, ***< 0.001, and ****< 0.0001.

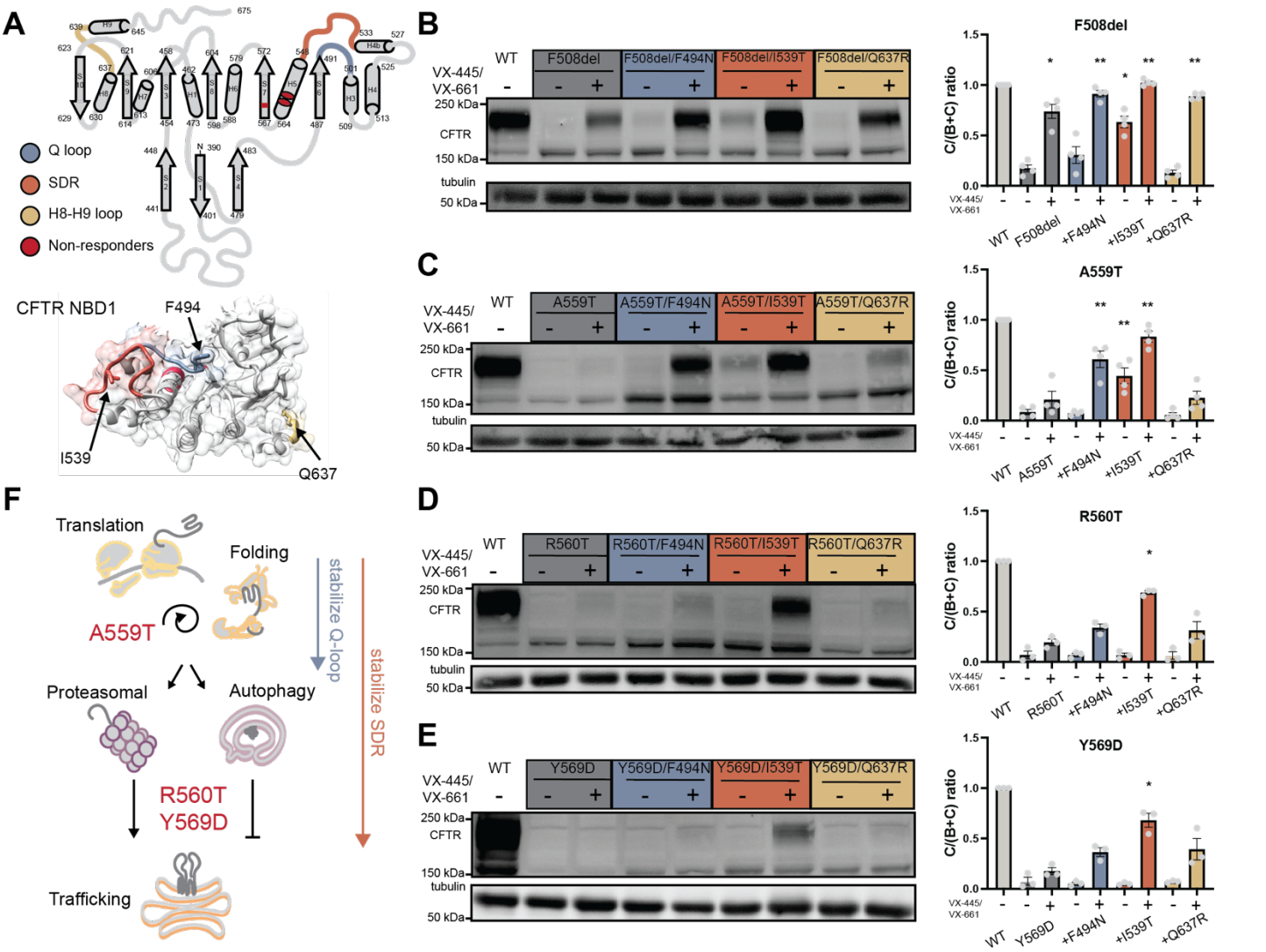

Figure 6. Stabilizing NBD1 with secondary mutations rescues poorly responsive variant trafficking.
A. Top: Ribbon diagram of the CFTR NBD1 structure with poor responders and loops susceptible to stabilizing secondary mutations highlighted. The Q-loop (residues 491-500) shown in blue, the SDR (residues 533-548) shown in orange, and the helix 8 – helix 9 (H8-H9) loop (residue 636-639) shown in gold. Bottom: CFTR NBD1 folded structure viewed from the NBD dimerizing face (5UAK[49]), F494, I539, and Q637 are depicted in their respective loops. This shows SDR and the Q-loop lying proximate to the poorly responsive variants (red), whereas the H8-H9 loop is on the other side of NBD1.
B. Representative Western blots and blot quantifications depicting F508del CFTR under basal and dual drug treatment conditions in combination with secondary stabilizing mutations F494N, I539T, and Q637R. WT CFTR is shown as a control. Quantification of C/(C+B) band ratio demonstrates dual 3 uM VX-445/VX-661 treatment and secondary mutation I539T rescues F508del. All secondary mutations F494N, I539T, and Q637R rescue F508del with drug.
C. Representative Western blots and quantifications depicting poorly responsive and trapped proteostasis variant A559T CFTR under basal and dual drug treatment conditions combined with secondary stabilizing mutations F494N, I539T, and Q637R. Quantification of C/(C+B) band ratio demonstrates secondary mutations F494N and I539T plus dual corrector treatment leads to drug response.
D-E. Representative western blots and blot quantifications depicting poorly responsive and productive proteostasis variants R560T and Y569D CFTR under basal and dual drug treatment conditions in combination with secondary stabilizing mutations F494N, I539T, and Q637R. WT CFTR is shown as a control. Quantifying the C/(C+B) band ratio demonstrates secondary mutations I539T combined with drug treatment rescues R560T

and Y569D trafficking. Statistical significances for **B.-E.** were calculated using a parametric ratio paired t-test, and p values were depicted by *< 0.05, **< 0.01, ***< 0.001, and ****< 0.0001.
F. The data suggests a model where A559T is trapped in the translation and folding stage of biogenesis even with dual corrector treatment, while R560T and Y569D escape this fate and proteasomal degradation with correctors but are still halted by autophagy degradation. Secondary mutation stabilization with F494N in the Q-loop allows A559T to escape trapped proteostasis and traffic efficiently, while I559T is sufficient to stabilize all variants to promote productive folding and trafficking.

REFERENCES

1. Veit, G. *et al.* From CFTR biology toward combinatorial pharmacotherapy: expanded classification of cystic fibrosis mutations. *Mol. Biol. Cell* **27**, 424–433 (2016).
2. McDonald, E. F., Meiler, J. & Plate, L. CFTR Folding: From Structure and Proteostasis to Cystic Fibrosis Personalized Medicine. *ACS Chem. Biol.* acschembio.3c00310 (2023) doi:10.1021/acschembio.3c00310.
3. Trikafta Prescribing Information. (2024).
4. CF Foundation Patient Registry, https://www.cff.org/medical-professionals/patient-registry. (2022).
5. Riordan, J. R. *et al.* Identification of the Cystic Fibrosis Gene: Cloning and Characterization of Complementary DNA. *Science* **245**, 1066–1073 (1989).
6. Fiedorczuk, K. & Chen, J. Mechanism of CFTR correction by type I folding correctors. *Cell* **185**, 158-168.e11 (2022).
7. Veit, G. *et al.* Structure-guided combination therapy to potently improve the function of mutant CFTRs. *Nat. Med.* **24**, 1732–1742 (2018).
8. Fiedorczuk, K. & Chen, J. Molecular structures reveal synergistic rescue of Δ508 CFTR by Trikafta modulators. *Science* **378**, 284–290 (2022).
9. Veit, G. *et al.* Allosteric folding correction of F508del and rare CFTR mutants by elexacaftor-tezacaftor-ivacaftor (Trikafta) combination. *JCI Insight* **5**, e139983 (2020).
10. McKee, A. G. *et al.* General trends in the effects of VX-661 and VX-445 on the plasma membrane expression of clinical CFTR variants. *Cell Chem. Biol.* **30**, 632-642.e5 (2023).
11. Pankow, S. *et al.* Δf508 CFTR interactome remodelling promotes rescue of cystic fibrosis. *Nature* **528**, 510–516 (2015).
12. Wang, X. *et al.* Hsp90 Cochaperone Aha1 Downregulation Rescues Misfolding of CFTR in Cystic Fibrosis. *Cell* **127**, 803–815 (2006).
13. McDonald, E. F., Sabusap, C. M. P., Kim, M. & Plate, L. Distinct proteostasis states drive pharmacologic chaperone susceptibility for cystic fibrosis transmembrane conductance regulator misfolding mutants. *Mol. Biol. Cell* **33**, ar62 (2022).
14. Kim, M. *et al.* Elexacaftor/VX-445–mediated CFTR interactome remodeling reveals differential correction driven by mutation-specific translational dynamics. *J. Biol. Chem.* **299**, 105242 (2023).
15. McKee, A. G. *et al.* General trends in the effects of VX-661 and VX-445 on the plasma membrane expression of clinical CFTR variants. *Cell Chem. Biol.* **30**, 632-642.e5 (2023).
16. Anglès, F., Wang, C. & Balch, W. E. Spatial covariance analysis reveals the residue-by-residue thermodynamic contribution of variation to the CFTR fold. *Commun. Biol.* **5**, 356 (2022).
17. Zacarias, S., Batista, M. S. P., Ramalho, S. S., Victor, B. L. & Farinha, C. M. Rescue of Rare CFTR Trafficking Mutants Highlights a Structural Location-Dependent Pattern for Correction. *Int. J. Mol. Sci.* **24**, 3211 (2023).
18. Kleinfelder, K. *et al.* Theratyping of the Rare CFTR Genotype A559T in Rectal Organoids and Nasal Cells Reveals a Relevant Response to Elexacaftor (VX-445) and Tezacaftor (VX-661) Combination. *Int. J. Mol. Sci.* **24**, 10358 (2023).
19. Roxo-Rosa, M. *et al.* Revertant mutants G550E and 4RK rescue cystic fibrosis mutants in the first nucleotide-binding domain of CFTR by different mechanisms. *Proc. Natl. Acad. Sci. U. S. A.* **103**, 17891–17896 (2006).
20. Bihler, H. *et al.* In vitro modulator responsiveness of 655 CFTR variants found in people with cystic fibrosis. *J. Cyst. Fibros.* S1569199324000213 (2024) doi:10.1016/j.jcf.2024.02.006.
21. Denning, G. M. *et al.* Processing of mutant cystic fibrosis transmembrane conductance regulator is temperature-sensitive. *Nature* **358**, 761–764 (1992).
22. Okiyoneda, T. *et al.* Role of calnexin in the ER quality control and productive folding of CFTR; differential effect of calnexin knockout on wild-type and ΔF508 CFTR. *Biochim. Biophys. Acta - Mol. Cell Res.* **1783**, 1585–1594 (2008).
23. Farinha, C. M. & Amaral, M. D. Most F508del-CFTR Is Targeted to Degradation at an Early Folding Checkpoint and Independently of Calnexin. *Mol. Cell. Biol.* **25**, 5242–5252 (2005).
24. Loureiro, C. A. *et al.* A molecular switch in the scaffold NHERF1 enables misfolded CFTR to evade the peripheral quality control checkpoint. *Sci. Signal.* **8**, ra48–ra48 (2015).

25. Arndt, V., Daniel, C., Nastainczyk, W., Alberti, S. & Höhfeld, J. BAG-2 Acts as an Inhibitor of the Chaperone-associated Ubiquitin Ligase CHIP. *Mol. Biol. Cell* **16**, 5891–5900 (2005).
26. Dai, Q. *et al.* Regulation of the Cytoplasmic Quality Control Protein Degradation Pathway by BAG2. *J. Biol. Chem.* **280**, 38673–38681 (2005).
27. Sondo, E. *et al.* Pharmacological Inhibition of the Ubiquitin Ligase RNF5 Rescues F508del-CFTR in Cystic Fibrosis Airway Epithelia. *Cell Chem. Biol.* **25**, 891-905.e8 (2018).
28. Huang, F., Kirkpatrick, D., Jiang, X., Gygi, S. & Sorkin, A. Differential Regulation of EGF Receptor Internalization and Degradation by Multiubiquitination within the Kinase Domain. *Mol. Cell* **21**, 737–748 (2006).
29. Yu, Y. *et al.* K29-linked ubiquitin signaling regulates proteotoxic stress response and cell cycle. *Nat. Chem. Biol.* **17**, 896–905 (2021).
30. Sumi, T., Matsumoto, K. & Nakamura, T. Specific Activation of LIM kinase 2 via Phosphorylation of Threonine 505 by ROCK, a Rho-dependent Protein Kinase. *J. Biol. Chem.* **276**, 670–676 (2001).
31. Maekawa, M. *et al.* Signaling from Rho to the Actin Cytoskeleton Through Protein Kinases ROCK and LIM-kinase. *Science* **285**, 895–898 (1999).
32. Mckee, C. M. *et al.* Elexacaftor–Tezacaftor–Ivacaftor for Cystic Fibrosis with a Single Phe508del Allele. 1–10 (2019) doi:10.1056/NEJMoa1908639.
33. Rosser, M. F. N., Grove, D. E., Chen, L. & Cyr, D. M. Assembly and Misassembly of Cystic Fibrosis Transmembrane Conductance Regulator: Folding Defects Caused by Deletion of F508 Occur Before and After the Calnexin-dependent Association of Membrane Spanning Domain (MSD) 1 and MSD2. *Mol. Biol. Cell* **20**, 2673–2683 (2008).
34. Westhoff, B., Chapple, J. P., Van Der Spuy, J., Höhfeld, J. & Cheetham, M. E. HSJ1 is a neuronal shuttling factor for the sorting of chaperone clients to the proteasome. *Curr. Biol.* **15**, 1058–1064 (2005).
35. Hutt, D. M. *et al.* FK506 binding protein 8 peptidylprolyl isomerase activity manages a late stage of cystic fibrosis transmembrane conductance regulator (CFTR) folding and stability. *J. Biol. Chem.* **287**, 21914–21925 (2012).
36. Chiaw, P. K. *et al.* Hsp70 and DNAJA2 limit CFTR levels through degradation. *PLoS ONE* **14**, 1–27 (2019).
37. Choo-Kang, L. R. & Zeitlin, P. L. Induction of HSP70 promotes ??F508 CFTR trafficking. *Am. J. Physiol. - Lung Cell. Mol. Physiol.* **281**, 58–68 (2001).
38. Coppinger, J. A. *et al.* A chaperone trap contributes to the onset of cystic fibrosis. *PLoS ONE* **7**, 17–19 (2012).
39. Loo, M. A. *et al.* Perturbation of Hsp90 interaction with nascent CFTR prevents its maturation and accelerates its degradation by the proteasome. *EMBO J.* **17**, 6879–6887 (1998).
40. Hutt, D. M. *et al.* Silencing of the Hsp70-specific nucleotide-exchange factor BAG3 corrects the F508del-CFTR variant by restoring autophagy. *J. Biol. Chem.* **293**, 13682–13695 (2018).
41. El Khouri, E., Le Pavec, G., Toledano, M. B. & Delaunay-Moisan, A. RNF185 is a novel E3 ligase of endoplasmic reticulum-associated degradation (ERAD) that targets cystic fibrosis transmembrane conductance regulator (CFTR). *J. Biol. Chem.* **288**, 31177–31191 (2013).
42. Farsad, K. *et al.* Generation of high curvature membranes mediated by direct endophilin bilayer interactions. *J. Cell Biol.* **155**, 193–200 (2001).
43. McDonald, E. F. *et al.* Structural Comparative Modeling of Multi-Domain F508del CFTR. *Biomolecules* **12**, 471 (2022).
44. Rabeh, W. M. *et al.* Correction of Both NBD1 Energetics and Domain Interface Is Required to Restore ΔF508 CFTR Folding and Function. *Cell* **148**, 150–163 (2012).
45. Mendoza, J. L. *et al.* Requirements for efficient correction of Δf508 CFTR revealed by analyses of evolved sequences. *Cell* **148**, 164–174 (2012).
46. Wang, C. *et al.* Integrated biophysical studies implicate partial unfolding of NBD1 of CFTR in the molecular pathogenesis of F508del cystic fibrosis. *Protein Sci.* **19**, 1932–1947 (2010).
47. Protasevich, I. *et al.* Thermal unfolding studies show the disease causing F508del mutation in CFTR thermodynamically destabilizes nucleotide-binding domain 1. *Protein Sci.* **19**, 1917–1931 (2010).
48. Zhang, Z., Liu, F. & Chen, J. Molecular structure of the ATP-bound, phosphorylated human CFTR. *Proc. Natl. Acad. Sci.* **115**, 12757–12762 (2018).

49. Liu, F., Zhang, Z., Csanády, L., Gadsby, D. C. & Chen, J. Molecular Structure of the Human CFTR Ion Channel. *Cell* **169**, 85–92 (2017).
50. Wang, R. Y.-R. *et al.* Automated structure refinement of macromolecular assemblies from cryo-EM maps using Rosetta. *eLife* **5**, e17219 (2016).
51. He, L. *et al.* Restoration of domain folding and interdomain assembly by second-site suppressors of the ΔF508 mutation in CFTR. *FASEB J.* **24**, 3103–3112 (2010).
52. Lewis, H. A. *et al.* Structure and dynamics of NBD1 from CFTR characterized using crystallography and hydrogen/deuterium exchange mass spectrometry. *J. Mol. Biol.* **396**, 406–430 (2010).
53. Yang, Z. *et al.* Structural stability of purified human CFTR is systematically improved by mutations in nucleotide binding domain 1. *Biochim. Biophys. Acta - Biomembr.* **1860**, 1193–1204 (2018).
54. Dawson, J. E., Farber, P. J. & Forman-Kay, J. D. Allosteric Coupling between the Intracellular Coupling Helix 4 and Regulatory Sites of the First Nucleotide-binding Domain of CFTR. *PLoS ONE* **8**, (2013).
55. McDonald, E. F., Oliver, K. E., Schlebach, J. P., Meiler, J. & Plate, L. Benchmarking AlphaMissense pathogenicity predictions against cystic fibrosis variants. *PLOS ONE* **19**, e0297560 (2024).
56. Carolyn Padoa, Andrea Goldman, Trefor Jenkins, & Michele Ramsay. Cystic fibrosis carrier frequencies in populations of African origin. *J. Med. Genet.* **36**, 41 (1999).
57. Zeiger, A. M. *et al.* Identification of CFTR variants in Latino patients with cystic fibrosis from the Dominican Republic and Puerto Rico. *Pediatr. Pulmonol.* **55**, 533–540 (2020).
58. Farinha, C. M. *et al.* Revertants, low temperature, and correctors reveal the mechanism of F508del-CFTR rescue by VX-809 and suggest multiple agents for full correction. *Chem. Biol.* **20**, 943–955 (2013).
59. Hurlbut, G. *et al.* EPS3.10 Novel CFTR modulator combinations directly address the ΔF508-CFTR NBD1 stability defect and enable full CFTR correction. *J. Cyst. Fibros.* **22**, S45 (2023).
60. Kim, M. & Plate, L. Cystic Fibrosis Modulator Therapies: Bridging Insights from CF to other Membrane Protein Misfolding Diseases. *Isr. J. Chem.* e202300152 (2024) doi:10.1002/ijch.202300152.
61. Sabusap, C. M. *et al.* Analysis of cystic fibrosis–associated P67L CFTR illustrates barriers to personalized therapeutics for orphan diseases. *JCI Insight* **1**, 1–10 (2016).
62. Welzel, T., Radtke, I., Meyer-Zaika, W., Heumann, R. & Epple, M. Transfection of cells with custom-made calcium phosphate nanoparticles coated with DNA. *J. Mater. Chem.* **14**, 2213 (2004).
63. Pankow, S., Bamberger, C., Calzolari, D., Bamberger, A. & Yates III, J. R. Deep interactome profiling of membrane proteins by co-interacting protein identification technology. *Nat. Protoc.* **11**, 2515–2515 (2016).
64. Mendenhall, J., Brown, B. P., Kothiwale, S. & Meiler, J. BCL::Conf: Improved Open-Source Knowledge-Based Conformation Sampling Using the Crystallography Open Database. *J. Chem. Inf. Model.* **61**, 189–201 (2021).
65. Lemmon, G. & Meiler, J. Rosetta Ligand Docking with Flexible XML Protocols. in *Computational Drug Discovery and Design* (ed. Baron, R.) vol. 819 143–155 (Springer New York, New York, NY, 2012).
66. Song, Y. *et al.* High-Resolution Comparative Modeling with RosettaCM. *Structure* **21**, 1735–1742 (2013).
67. Yarov-Yarovoy, V., Schonbrun, J. & Baker, D. Multipass membrane protein structure prediction using Rosetta. *Proteins Struct. Funct. Bioinforma.* **62**, 1010–1025 (2006).
68. Barth, P., Schonbrun, J. & Baker, D. Toward high-resolution prediction and design of transmembrane helical protein structures. *Proc. Natl. Acad. Sci.* **104**, 15682–15687 (2007).
69. Viklund, H. & Elofsson, A. OCTOPUS: improving topology prediction by two-track ANN-based preference scores and an extended topological grammar. *Bioinformatics* **24**, 1662–1668 (2008).
70. Shishido, H., Yoon, J. S., Yang, Z. & Skach, W. R. CFTR trafficking mutations disrupt cotranslational protein folding by targeting biosynthetic intermediates. *Nat. Commun.* **11**, 4258–4258 (2020).

Supplementary Information

for

Proteostasis Landscapes of Selective versus Poorly Responsive CFTR Variants Reveals Structural Vulnerabilities to Correction

Eli Fritz McDonald[1,2], Minsoo Kim[1,3], John A Olson III[1,3], Jens Meiler[1,2,4,5,*], Lars Plate[1,6,7,*]

[1]Department of Chemistry, Vanderbilt University, Nashville, TN 37235, USA
[2]Center for Structural Biology, Vanderbilt University, Nashville, TN 37240, USA
[3]Chemical and Physical Biology Program, Vanderbilt University, Nashville, TN 37240, USA
[4]Department of Pharmacology, Vanderbilt University, Nashville, TN 37240, USA
[5]Institute for Drug Discovery, Leipzig University, Leipzig, SAC 04103, Germany
[6]Department of Biological Sciences, Vanderbilt University, Nashville, TN 37235, USA
[7]Department of Pathology, Microbiology and Immunology, Vanderbilt University Medical Center, Nashville, TN 37232, USA

* Corresponding authors: JM (jens@meilerlab.org), LP (lars.plate@vanderbilt.edu)

Table of Contents

Supplementary Table S1……..2

Supplementary Figures S1-S9……...……..2-17

References…….……...……..18

Supplemental Table S1. Allele frequencies of poorly-responsive CFTR variants[1].

Allele	# of Patients	w/ F508del	w/o F508del
V520F	155	105	50
L558S	33	19	14
A559T	85	39	46
R560T	340	243	97
A561E	15	7	8
Y569D	28	2	26
R1066C	211	124	87
Total	867		**328**

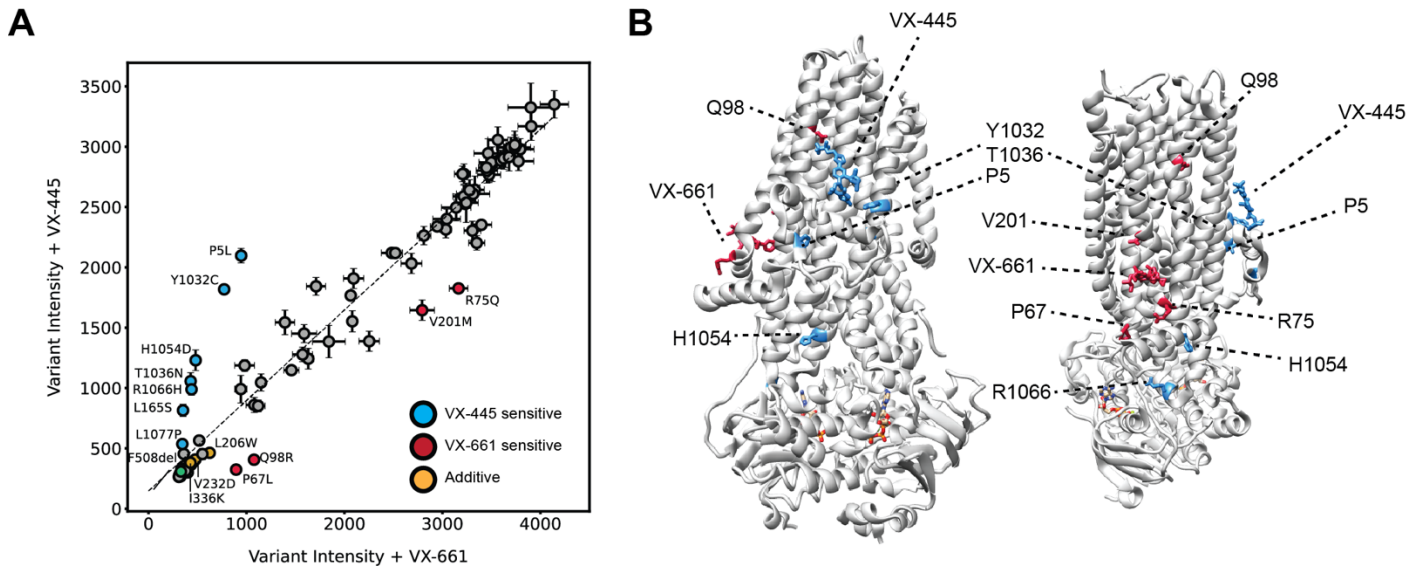

Supplementary Figure S1. Deep mutational scanning reveals selective sensitivity of CFTR variants with VX-661 and VX-445.

A. Adapted from Figure 3B in[2] CFTR cell surface immune staining intensity comparing treatment with VX-661 versus VX-445 correctors with the best fit dotted line representing equivalent response to both correctors. Variants that fell below the best-fit dotted line were selectively responsive to VX-661, while variants above the dotted line were selectively responsive to VX-445. Selectively sensitive variants were annotated. Error bars represent standard deviations.

B. CFTR structure (PDB ID 8EIQ)[3] showing VX-445 sensitive variants proximate to the VX-445 binding site (blue) as well as VX-661 sensitive variants proximate to the VX-661 binding site (red).

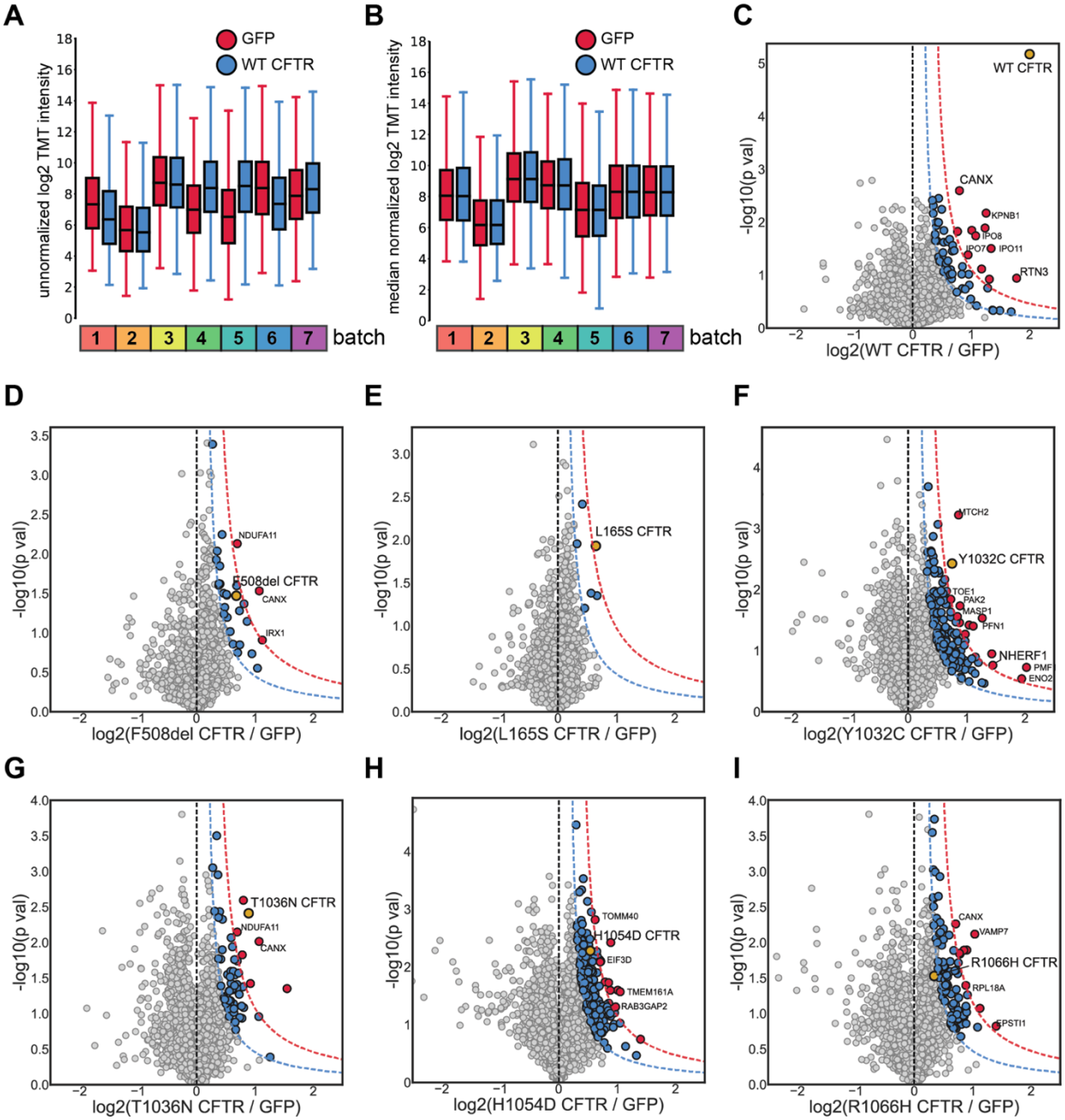

Supplemental Figure S2. Identification of statistically significant interactors with VX-445 responsive CFTR variants under basal (DMSO) conditions.

A. Box and whisker plot showing the unnormalized TMT channel intensity distributions of GFP mock control and WT CFTR for all 7 LC-MS/MS runs included in the selectively responsive variants dataset. The box limits represent the upper and lower quartiles with a line at the median; the whiskers represent the limits 1.5 times the interquartile range.

B. Box and whisker plot showing the corresponding median normalized TMT channel intensity distributions of GFP mock control and WT CFTR for the 7 LC-MS/MS run. Median normalization of TMT quantification for a given run results int the median of each run for different conditions, e.g. GFP and WT shown here, approximately equal. Box plots represented the same as in A.

C. Volcano plot of WT interactors. Interactors were identified using a curved cutoff at 0.5σ for medium confidence (blue) and 1σ for high confidence (red) proteins; CFTR shown in gold. Interacting proteins across selectively responsive variants were added to a master list comprising 655 interactors for this data set.

D. Volcano plot of F508del + DMSO interactors. Interactors were identified using a curved cutoff at 0.5σ for medium confidence (blue) and 1σ for high confidence (red) proteins; CFTR shown in gold.
E. Volcano plot of L165S + DMSO interactors. Interactors were identified using a curved cutoff at 0.5σ for medium confidence (blue) and 1σ for high confidence (red) proteins, CFTR shown in gold. Of note, L165S fails to enrich many interactors compared to other selectively responsive variants.
F. Volcano plot of Y1032C + DMSO interactors. Interactors were identified using a curved cutoff at 0.5σ for medium confidence (blue) and 1σ for high confidence (red) proteins, CFTR shown in gold.
G. Volcano plot of T1036N + DMSO interactors. Interactors were identified using a curved cutoff at 0.5σ for medium confidence (blue) and 1σ for high confidence (red) proteins, CFTR shown in gold.
H. Volcano plot of H1054D + DMSO interactors. Interactors were identified using a curved cutoff at 0.5σ for medium confidence (blue) and 1σ for high confidence (red) proteins, CFTR shown in gold.
I. Volcano plot of R1066H + DMSO interactors. Interactors were identified using a curved cutoff at 0.5σ for medium confidence (blue) and 1σ for high confidence (red) proteins, CFTR shown in gold.

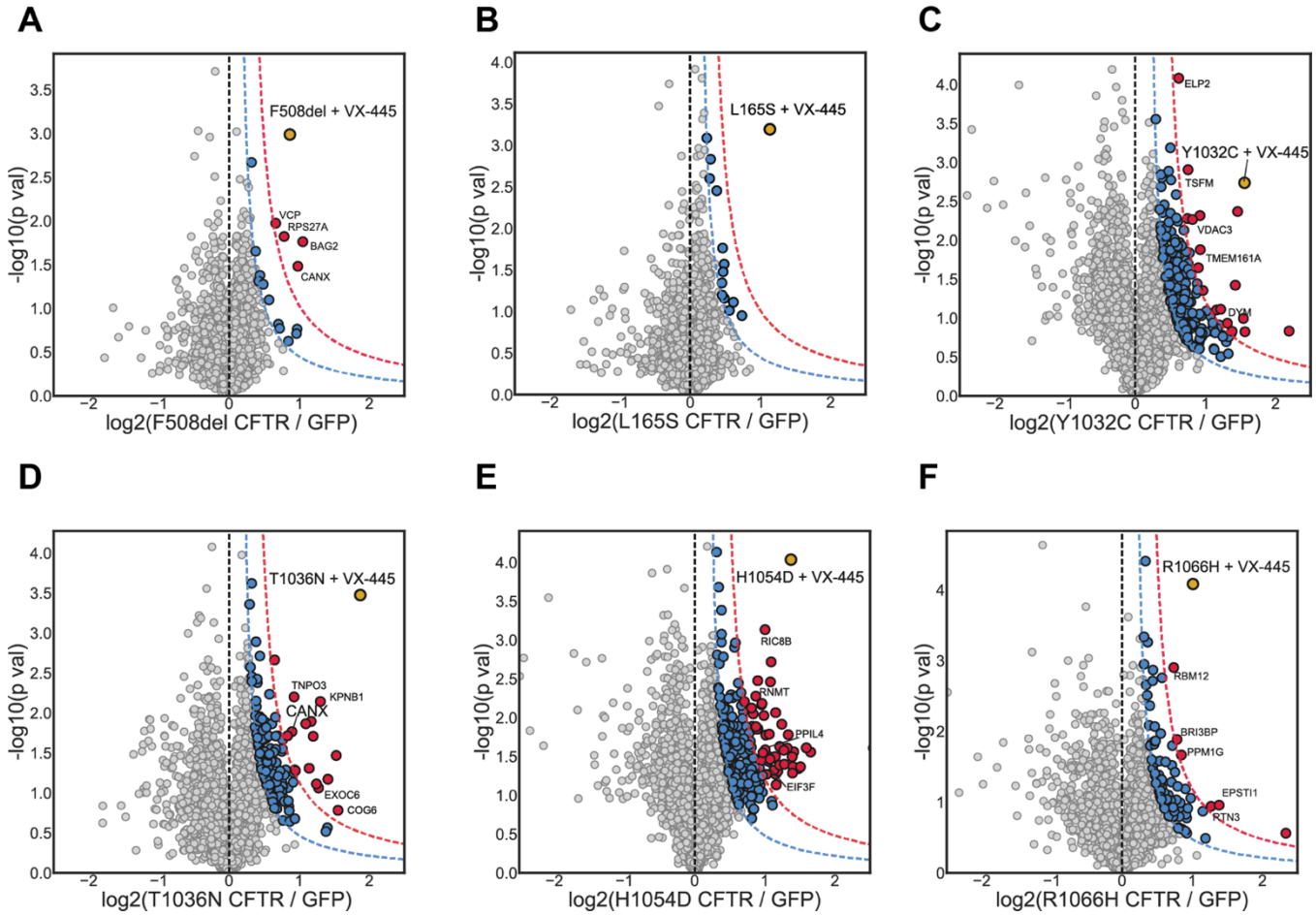

Supplemental Figure S3. Identification of statistically significant interactors with VX-445 responsive CFTR variants under drug treatment (3 µM VX-445) conditions.

A. Volcano plot of F508del + VX-445 interactors. Interactors were identified using a curved cutoff at 0.5σ for medium confidence (blue) and 1σ for high confidence (red) proteins, CFTR shown in gold. Interacting proteins across selectively responsive variants were added to a master list comprising 655 interactors for this data set.

B. Volcano plot of L165S + VX-445 interactors. Interactors were identified using a curved cutoff at 0.5σ for medium confidence (blue) and 1σ for high confidence (red) proteins, CFTR shown in gold. L165S interactors identified.

C. Volcano plot of Y1032C + VX-445 interactors. Interactors were identified using a curved cutoff at 0.5σ for medium confidence (blue) and 1σ for high confidence (red) proteins, CFTR shown in gold.

D. Volcano plot of T1036N + VX-445 interactors. Interactors were identified using a curved cutoff at 0.5σ for medium confidence (blue) and 1σ for high confidence (red) proteins, CFTR shown in gold.

E. Volcano plot of H1054D + VX-445 interactors. Interactors were identified using a curved cutoff at 0.5σ for medium confidence (blue) and 1σ for high confidence (red) proteins, CFTR shown in gold.

F. Volcano plot of R1066H + VX-445 interactors. Interactors were identified using a curved cutoff at 0.5σ for medium confidence (blue) and 1σ for high confidence (red) proteins, CFTR shown in gold.

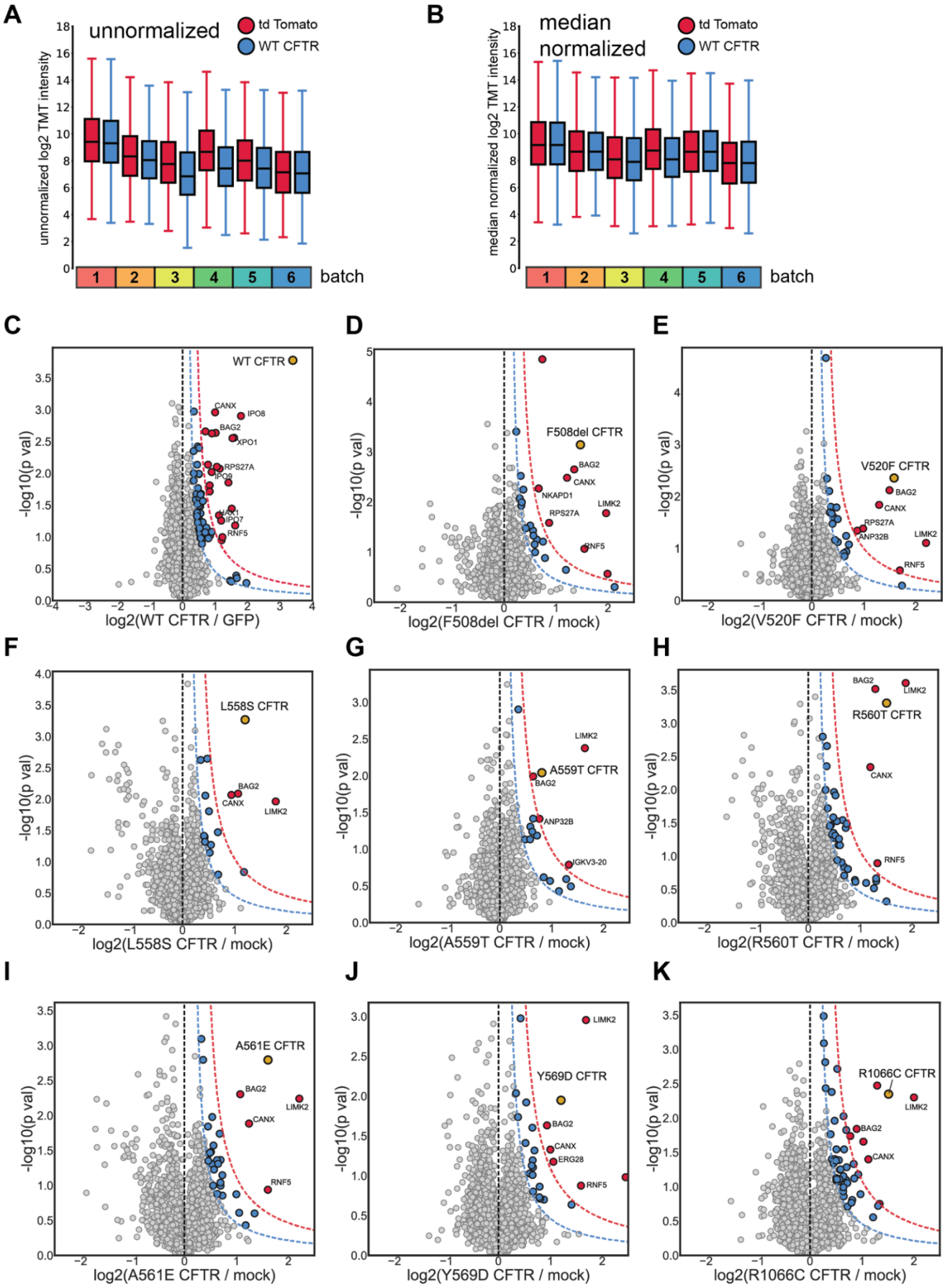
A
unnormalized
td Tomato
WT CFTR
unnormalized log2 TMT intensity
batch
B
median normalized
td Tomato
WT CFTR
median normalized log2 TMT intensity
batch
C
WT CFTR
CANX
IPO8
BAG2
XPO1
RPS27A
IPO9
IPO7
RNF5
-log10(p val)
log2(WT CFTR / GFP)
D
F508del CFTR
BAG2
CANX
NKAPD1
LIMK2
RPS27A
RNF5
-log10(p val)
log2(F508del CFTR / mock)
E
V520F CFTR
BAG2
CANX
RPS27A
ANP32B
LIMK2
RNF5
-log10(p val)
log2(V520F CFTR / mock)
F
L558S CFTR
BAG2
CANX
LIMK2
-log10(p val)
log2(L558S CFTR / mock)
G
LIMK2
A559T CFTR
BAG2
ANP32B
IGKV3-20
-log10(p val)
log2(A559T CFTR / mock)
H
BAG2
LIMK2
R560T CFTR
CANX
RNF5
-log10(p val)
log2(R560T CFTR / mock)
I
A561E CFTR
BAG2
LIMK2
CANX
RNF5
-log10(p val)
log2(A561E CFTR / mock)
J
LIMK2
Y569D CFTR
BAG2
CANX
ERG28
RNF5
-log10(p val)
log2(Y569D CFTR / mock)
K
R1066C CFTR
LIMK2
BAG2
CANX
-log10(p val)
log2(R1066C CFTR / mock)

Supplemental Figure S4. Identification of statistically significant interactors with poorly-responsive CFTR variants under basal conditions.

A. Box and whisker plot showing the unnormalized TMT channel intensity distributions of tdTomato mock control and WT CFTR for all 6 LC-MS/MS runs included in the selectively responsive variants dataset. The box limits represent the upper and lower quartiles with a line at the median; the whiskers represent the limits 1.5 times the interquartile range.

B. Box and whisker plot showing the median normalized TMT channel intensity distributions of td-Tomato mock control and WT CFTR for the corresponding 6 LC-MS/MS run. Median normalization of TMT quantification for a given run results int the median of each run for different conditions, e.g. td-Tomato and WT shown here, approximately equal. Box plots represented the same as in A.

C. Volcano plot of WT CFTR interactors. Interactors were identified using a curved cutoff at 0.5σ for medium confidence (blue) and 1σ for high confidence (red) proteins, CFTR shown in gold. Interacting proteins across poorly-responsive variants and controls were added to a master list comprising 284 interactors for this data set.

D. Volcano plot of F508del CFTR + DMSO interactors. Interactors were identified using a curved cutoff at 0.5σ for medium confidence (blue) and 1σ for high confidence (red) proteins, CFTR shown in gold.

E. Volcano plot of V520F CFTR + DMSO interactors. Interactors were identified using a curved cutoff at 0.5σ for medium confidence (blue) and 1σ for high confidence (red) proteins, CFTR shown in gold.

F. Volcano plot of L558S CFTR + DMSO interactors. Interactors were identified using a curved cutoff at 0.5σ for medium confidence (blue) and 1σ for high confidence (red) proteins, CFTR shown in gold.

G. Volcano plot of A559T CFTR + DMSO interactors. Interactors were identified using a curved cutoff at 0.5σ for medium confidence (blue) and 1σ for high confidence (red) proteins, CFTR shown in gold.

H. Volcano plot of R560T CFTR + DMSO interactors. Interactors were identified using a curved cutoff at 0.5σ for medium confidence (blue) and 1σ for high confidence (red) proteins, CFTR shown in gold.

I. Volcano plot of A561E CFTR+ DMSO interactors. Interactors were identified using a curved cutoff at 0.5σfor medium confidence (blue) and 1σ for high confidence (red) proteins, CFTR shown in gold.

J. Volcano plot of Y569D CFTR + DMSO interactors. Interactors were identified using a curved cutoff at 0.5σ for medium confidence (blue) and 1σ for high confidence (red) proteins, CFTR shown in gold.

K. Volcano plot of R1066C CFTR + DMSO interactors. Interactors were identified using a curved cutoff at 0.5σ for medium confidence (blue) and 1σ for high confidence (red) proteins, CFTR shown in gold.

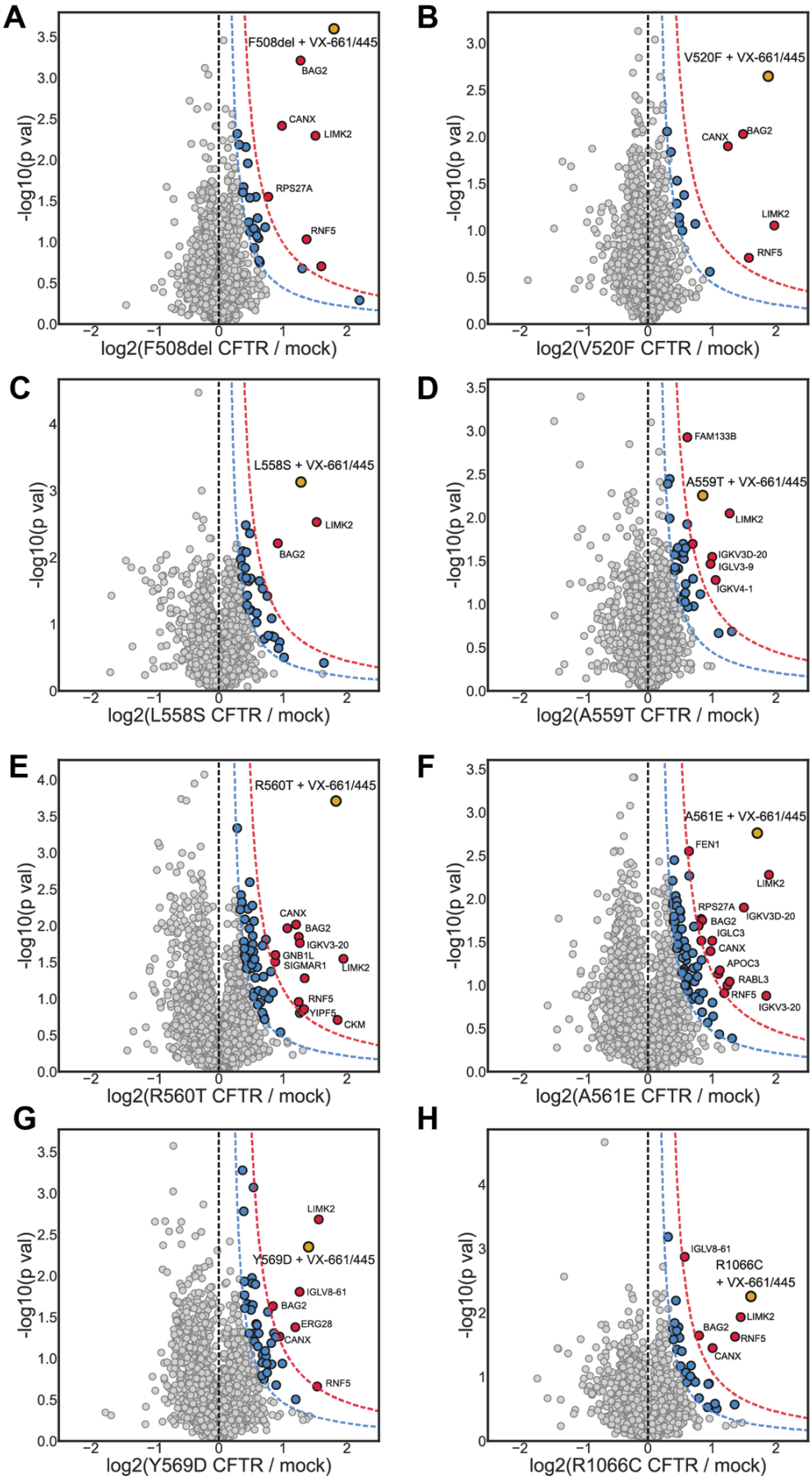
A
F508del + VX-661/445
BAG2
CANX
LIMK2
RPS27A
RNF5
-log10(p val)
log2(F508del CFTR / mock)
B
V520F + VX-661/445
CANX
BAG2
LIMK2
RNF5
-log10(p val)
log2(V520F CFTR / mock)
C
L558S + VX-661/445
LIMK2
BAG2
-log10(p val)
log2(L558S CFTR / mock)
D
FAM133B
A559T + VX-661/445
LIMK2
IGKV3D-20
IGLV3-9
IGKV4-1
-log10(p val)
log2(A559T CFTR / mock)
E
R560T + VX-661/445
CANX
BAG2
IGKV3-20
GNB1L
SIGMAR1
LIMK2
RNF5
YIPF5
CKM
-log10(p val)
log2(R560T CFTR / mock)
F
A561E + VX-661/445
FEN1
LIMK2
RPS27A
IGKV3D-20
BAG2
IGLC3
CANX
APOC3
RABL3
RNF5
IGKV3-20
-log10(p val)
log2(A561E CFTR / mock)
G
LIMK2
Y569D + VX-661/445
IGLV8-61
BAG2
ERG28
CANX
RNF5
-log10(p val)
log2(Y569D CFTR / mock)
H
IGLV8-61
R1066C
+ VX-661/445
LIMK2
BAG2
RNF5
CANX
-log10(p val)
log2(R1066C CFTR / mock)

Supplemental Figure S5. Identification of statistically significant interactors with poorly-responsive CFTR variants under drug treatment (3 μM VX-661 + 3 μM VX-445) conditions.

A. Volcano plot of F508del CFTR + 3 μM VX-661 + 3 μM VX-445 interactors. Interactors were identified using a curved cutoff at 0.5σ for medium confidence (blue) and 1σ for high confidence (red) proteins, CFTR shown in gold.

B. Volcano plot of V520F CFTR + 3 μM VX-661 + 3 μM VX-445 interactors. Interactors were identified using a curved cutoff at 0.5σ for medium confidence (blue) and 1σ for high confidence (red) proteins, CFTR shown in gold.

C. Volcano plot of L558S CFTR + 3 μM VX-661 + 3 μM VX-445 interactors. Interactors were identified using a curved cutoff at 0.5σ for medium confidence (blue) and 1σ for high confidence (red) proteins, CFTR shown in gold.

D. Volcano plot of A559T CFTR + 3 μM VX-661 + 3 μM VX-445 interactors. Interactors were identified using a curved cutoff at 0.5σ for medium confidence (blue) and 1σ for high confidence (red) proteins, CFTR shown in gold.

E. Volcano plot of R560T CFTR + 3 μM VX-661 + 3 μM VX-445 interactors. Interactors were identified using a curved cutoff at 0.5σ for medium confidence (blue) and 1σ for high confidence (red) proteins, CFTR shown in gold.

F. Volcano plot of A561E CFTR + 3 μM VX-661 + 3 μM VX-445 interactors. Interactors were identified using a curved cutoff at 0.5σ for medium confidence (blue) and 1σ for high confidence (red) proteins, CFTR shown in gold.

G. Volcano plot of Y569D CFTR + 3 μM VX-661 + 3 μM VX-445 interactors. Interactors were identified using a curved cutoff at 0.5σ for medium confidence (blue) and 1σ for high confidence (red) proteins, CFTR shown in gold.

H. Volcano plot of R1066C CFTR + 3 μM VX-661 + 3 μM VX-445 interactors. Interactors were identified using a curved cutoff at 0.5σ for medium confidence (blue) and 1σ for high confidence (red) proteins, CFTR shown in gold.

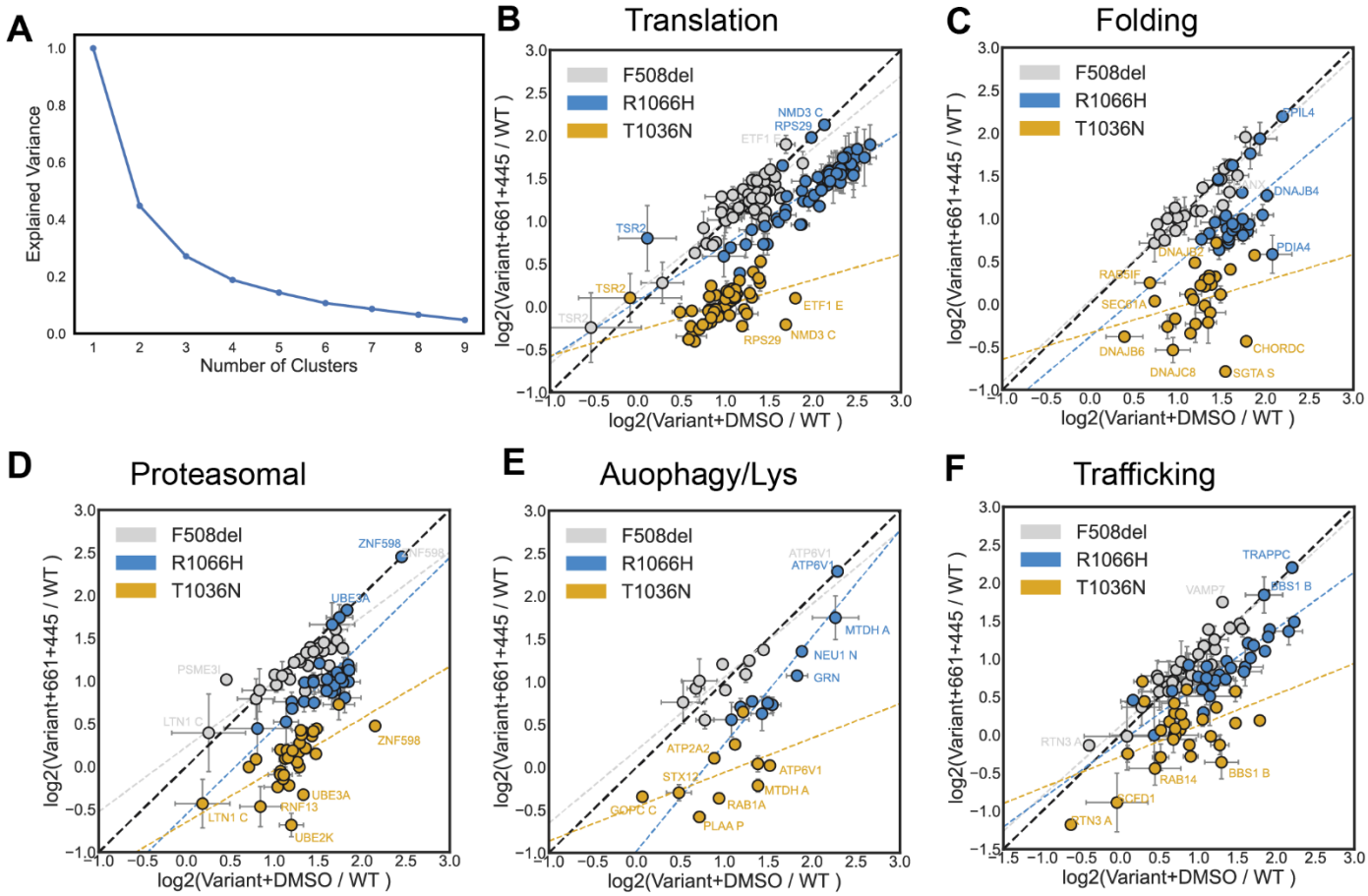

Supplemental Figure S6. Correlation between DMSO and 3 µM VX-445 protein interactor quantification levels organized by pathway for VX-445 selectively responsive CFTR variants.

A. Elbow plot of K means clustering cluster number versus explained variance for 655 interactors across all selectively responsive variants. The inflection point of the curve (elbow) occurs between 4 and 6 clusters; hence, we chose 5 clusters to cluster the Spearman rank order correlation heatmap in **Figure 3A**.

B.-F. Individual protein quantification correlation between DMSO and VX-445 treatment for F508del (grey), T1036N (gold), and R1066H (blue) for proteostasis pathways. A normal line (black dotted line) represents x=y or no change with the drug. A least squared linear best fit dotted line colored for each variant represented the off-normal axis behavior for each variant during drug treatment.

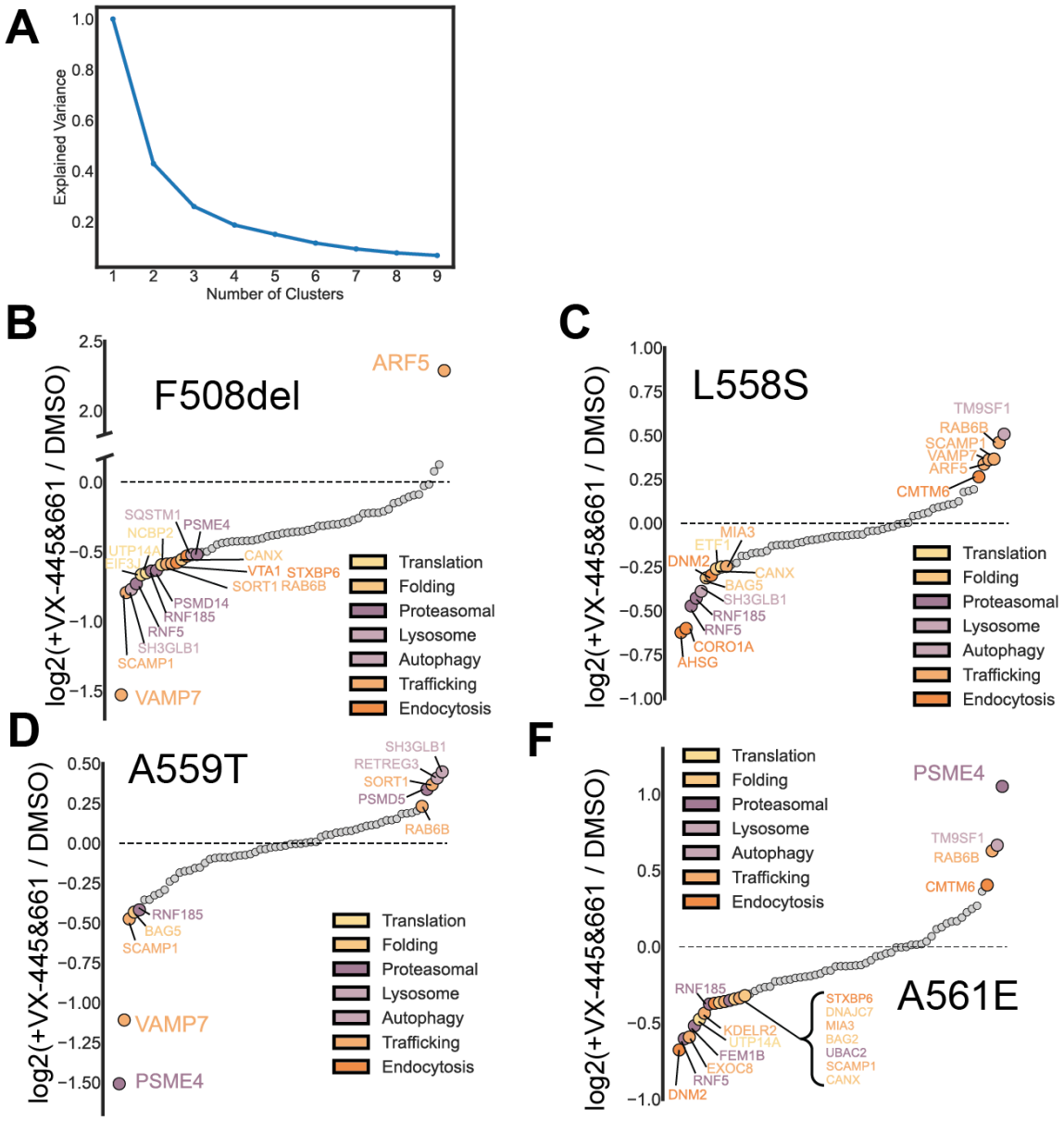

Supplemental Figure S7. Clustering poorly-responsive variants.

A. Elbow plot of K means clustering cluster number versus explained variance for 284 interactors across all selectively responsive variants. The curve's inflection point (elbow) occurs between 5 and 7 clusters; hence, we chose 6 clusters to cluster the Spearman rank order correlation heatmap in **Figure 4A**.

B. A waterfall plot of the log2 fold change between F508del + 3 μM VX-661/3 μM VX-445 over F508del + DMSO organized by fold change rank order. Interactors above zero are greater with drug treatment, and interactors under zero are greater in the basal state. Interactors greater than one-half a standard deviation of positive values are colored by pathway; likewise, for interactors less than one-half a standard deviation of negative values.

C-F. A waterfall plot of the log2 fold change between poorly-responsive variants + 3 μM VX-661/3 μM VX-445 over respective variant + DMSO organized by fold change rank order and color by pathway as in **B**.

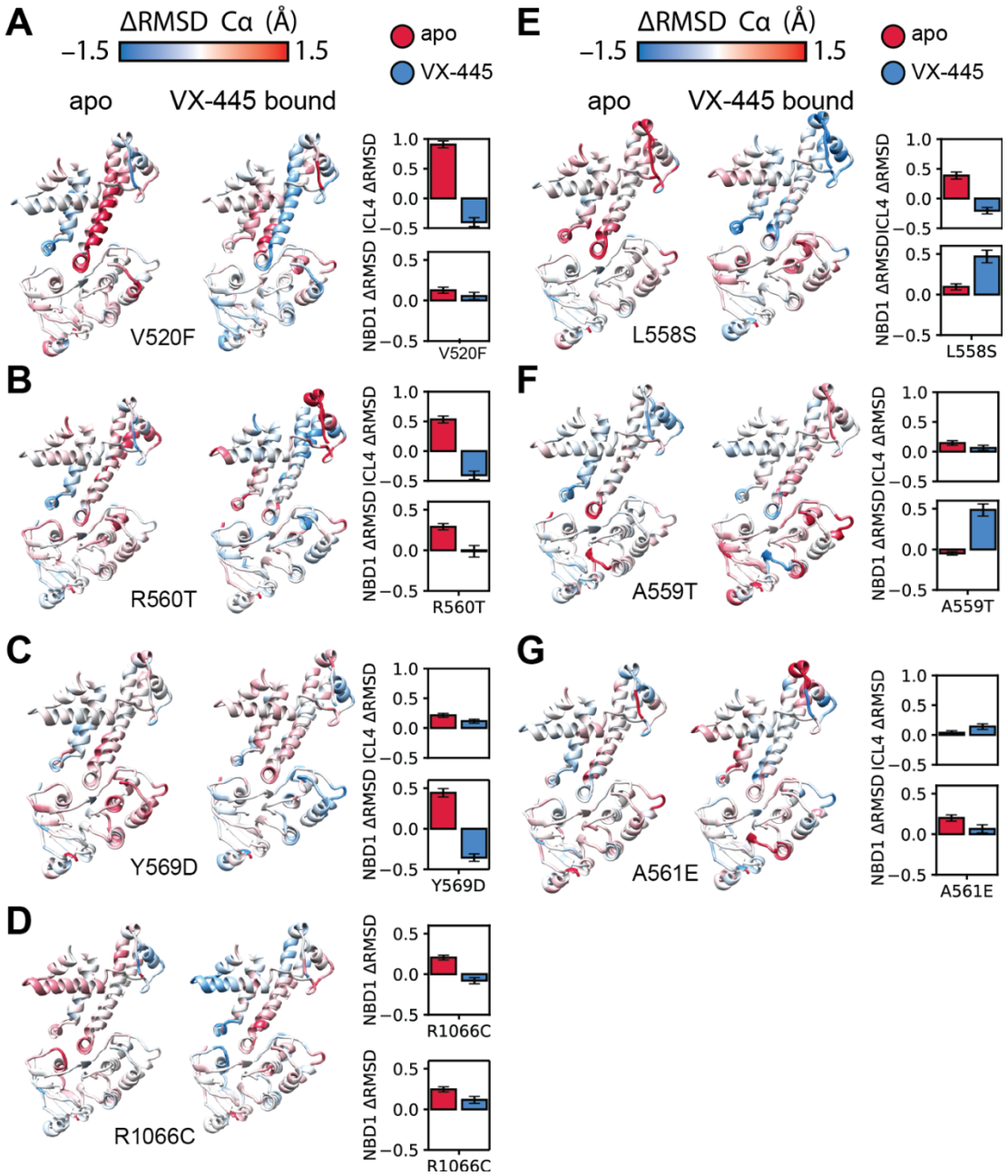

Supplemental Figure S8. Inactive structural modeling data in the apo and VX-445 bound state for poorly-responsive variants.

A. Poorly-responsive V520F ΔRMSD in the inactive conformation mapped onto CFTR structure, ICL1, ICL4, lasso motif, and NBD1 shown for clarity and ILC4 and NBD1 (residues 485-572) ΔRMSD in the inactive conformation quantification. The left structure labeled apo represents the ensemble RMSD in the inactive conformation of V520F (lowest 10% of models) minus the ensemble RMSD of WT CFTR (lowest 10% of models). The right structure labeled VX-445 bound represents the ensemble RMSD of V520F + VX-445 minus the ensemble RMSD of V520F apo. The bar graph shows the average, unnormalized ensemble RMSD for the apo and VX-445 bound V520F models.

B-G. Poorly-responsive R560T apo ΔRMSD in the inactive conformation normalized to WT (left) and VX-445 bound ΔRMSD in the inactive conformation normalized to apo R560T mapped onto CFTR ICL1/4, lasso, and NBD1. ΔRMSD quantification for ICL4 and NBD1 (485-572) is shown as a bar graph. **C.** Y656D ΔRMSD. **D.** R1066C ΔRMSD. **E.** L558S ΔRMSD. **F.** A559T ΔRMSD. **G.** A561E ΔRMSD.

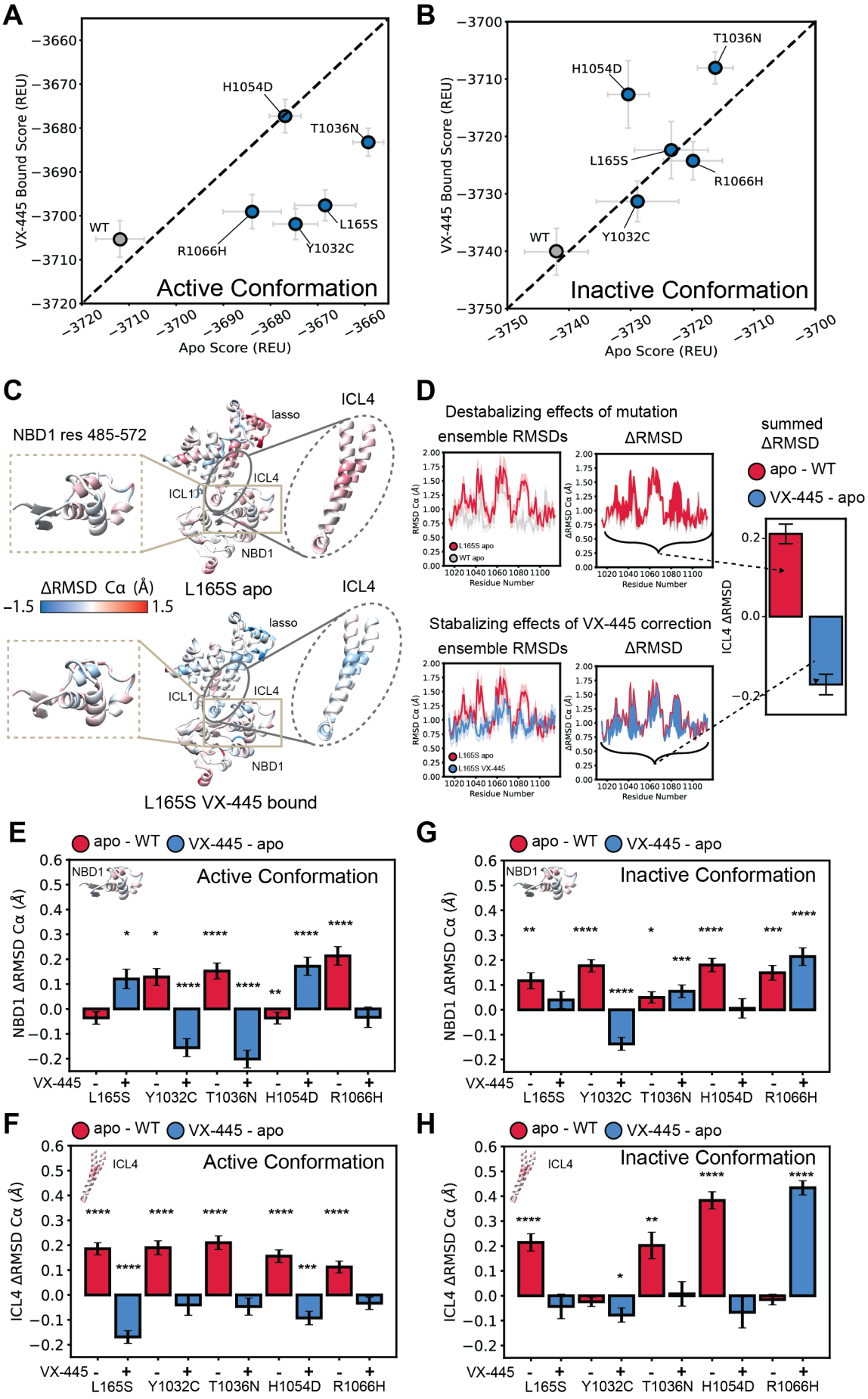
A
VX-445 Bound Score (REU)
Apo Score (REU)
H1054D
T1036N
WT
R1066H
Y1032C
L165S
Active Conformation
B
VX-445 Bound Score (REU)
Apo Score (REU)
T1036N
H1054D
L165S
R1066H
WT
Y1032C
Inactive Conformation
C
NBD1 res 485-572
lasso
ICL4
ICL1
NBD1
ΔRMSD Cα (Å)
−1.5
1.5
L165S apo
L165S VX-445 bound
D
Destabalizing effects of mutation
ensemble RMSDs
ΔRMSD
summed ΔRMSD
apo - WT
VX-445 - apo
Stabalizing effects of VX-445 correction
Residue Number
ICL4 ΔRMSD
E
apo - WT
VX-445 - apo
NBD1
Active Conformation
NBD1 ΔRMSD Cα (Å)
VX-445
L165S
Y1032C
T1036N
H1054D
R1066H
G
Inactive Conformation
F
ICL4
Active Conformation
ICL4 ΔRMSD Cα (Å)
H
Inactive Conformation

Supplemental Figure S9. RosettaCM bound to VX-445 versus apo state reveals the structural basis of VX-445 selective response.

A. The average Rosetta energy scores of the active conformation VX-445-bound state are plotted against the apo state CFTR models for responsive variants considered in this study. A dotted black line with a slope of one intersecting the origin (no effect) is shown for reference. Points represent the average Rosetta energy score, and the error bars represent the standard error of the mean across the 100 lowest (10%) energy-scoring models from an ensemble of 1000 active state models generated for each variant. VX-445 stabilized variants falling below the dotted line.

B. The average Rosetta energy scores of the inactive conformation VX-445-bound state are plotted against the apo state selectively responsive CFTR variants models. Points represent the average Rosetta energy score, and the error bars represent the standard error of the mean.

C. Comparison of variant instability and VX-445 conferred stability. On top, the ΔRMSD between apo L165S and WT CFTR in the active conformation was mapped onto PDB ID 6MSM[53]. On the bottom, the ΔRMSD between VX-445 bound L165S and apo L165S CFTR in the active conformation was mapped onto PDB ID 6MSM[53]. Intercellular Loop 1 (ICL1), ICL4, Lasso motif, and NBD1 are shown for clarity. NBD1 ΔRMSD (residues 485-572) were regarded because they contact TMD2 via ICL4, and ICL4 was also quantified.

D. Quantification of average ΔRMSD in ICL4 as an example calculation. On top, the ensemble RMSD by residue is shown for apo L165S and WT CFTR, followed by a plot showing the ΔRMSD between the RMSDs shaded in red. This represents the instability caused by the L165S mutation in ICL4. On the bottom, the ensemble RMSD by residue is shown for VX-445 bound L165S and apo L165S CFTR, followed by a plot showing the ΔRMSD between the RMSDs shaded in blue. This represents the stability conferred by VX-445 to L165S CFTR in ICL4. Both ΔRMSD values are summed in the quantification bar plot shown at the end and in **E-H** below.

E. ΔRMSD of NBD1 residues 485-572 for selectively responsive variants in the active conformation. Error bars represent the standard error of the mean, and colored as in **D.** Statistical significance was calculated using a non-parametric Wilcoxon signed-rank test compared to zero to determine if distributions were significantly different from zero, and p values were depicted by *< 0.05, **< 0.01, ***< 0.001, and ****< 0.0001.

F. ΔRMSD of ICL4 for selectively responsive variants in the active conformation. High ΔRMSD changes suggest VX-445 confers substantial stability to ICL4 in the active conformation. Error bars represent the standard error of the mean, and colored as in **D.**

G. ΔRMSD of NBD1 residues 485-572 for selectively responsive variants in the inactive conformation. Error bars represent the standard error of the mean, and colored as in **D.**

H. ΔRMSD of ICL4 for selectively responsive variants in the inactive conformation. Error bars represent the standard error of the mean, and colored as in **D.**

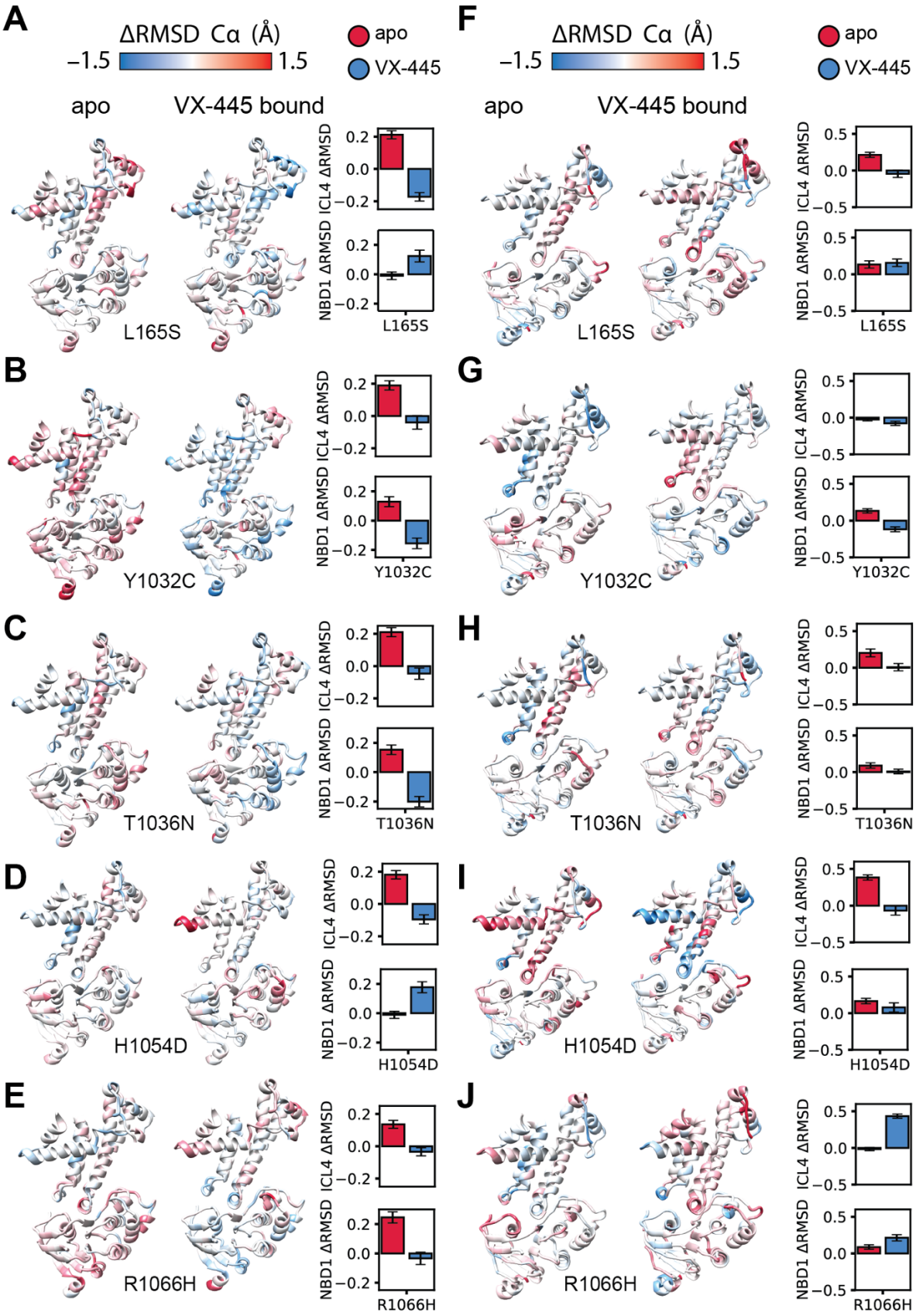

Supplemental Figure S10. Active and inactive state structural modeling data of the apo and VX-445 bound selectively responsive variants.

A. Selectively responsive L165S ΔRMSD in the active conformation mapped onto CFTR structure 6MSM, ICL1, ICL4, Lasso motif, and NBD1. The left structure labeled apo represents the ensemble RMSD in the active

conformation of L165S (lowest 10% of models) minus the ensemble RMSD of WT CFTR (lowest 10% of models). The right structure labeled VX-445 bound represents the ensemble RMSD of L165S + VX-445 minus the ensemble RMSD of L165S apo. The bar graph shows the ΔRMSD for ICL4 and NBD1 (residues 485-572) which contact TMD2.

B-E. Selectively responsive apo/WT ΔRMSD in the active conformation (left) and VX-445 bound/apo ΔRMSD in the active conformation mapped onto CFTR 6MSM ICL1/4, lasso, and NBD1. ΔRMSD quantification for ICL4 and NBD1 (residues 485-572) which contact TMD2. **B.** Active state Y1032C ΔRMSD. **C.** Active state T1036N ΔRMSD. **D.** Active state H1054D ΔRMSD. **E.** Active state R1066H ΔRMSD.

F-J. Selectively responsive apo/WT ΔRMSD in the inactive conformation (left) and VX-445 bound/apo ΔRMSD in the active conformation mapped onto CFTR 5uak ICL1/4, lasso, and NBD1. ΔRMSD quantification for ICL4 and NBD1 (residues 485-572) which contact TMD2. **F.** Inactive state L165S ΔRMSD. **G.** Inactive state Y1032C ΔRMSD. **H.** Inactive state T1036N ΔRMSD. **I.** Inactive state H1054D ΔRMSD. **J.** Inactive state R1066H ΔRMSD.

References

1. The Clinical and Functional TRanslation of CFTR (CFTR2); available at http://cftr2.org.
2. McKee, A. G. *et al.* General trends in the effects of VX-661 and VX-445 on the plasma membrane expression of clinical CFTR variants. *Cell Chem. Biol.* **30**, 632-642.e5 (2023).
3. Fiedorczuk, K. & Chen, J. Molecular structures reveal synergistic rescue of Δ508 CFTR by Trikafta modulators. *Science* **378**, 284–290 (2022).